biomass

MDPI

Review

Biomass-Derived Advanced Carbon-Based Electrocatalysts for Oxygen Reduction Reaction

Srijib Das [1], Souvik Ghosh [1,2], Tapas Kuila [1,2], Naresh Chandra Murmu [1,2] and Aniruddha Kundu [1,*]

[1] Surface Engineering and Tribology Division, Council of Scientific and Industrial Research Central Mechanical Engineering Research Institute, Mahatma Gandhi Avenue, Durgapur 713209, West Bengal, India
[2] Academy of Scientific and Innovative Research (AcSIR), CSIR-Human Resource Development Centre, (CSIR-HRDC) Campus, Postal Staff College Area, Sector 19, Kamla Nehru Nagar, Ghaziabad 201002, Uttar Pradesh, India
* Correspondence: write2aknow@gmail.com

Abstract: Noble metal-based materials are enormously used as a cathode material for electrocatalytic oxygen reduction reaction (ORR), which plays an important role in determining the performance of energy conversion and storage devices such as fuel cells, metal-air battery, and so on. The practicability of these energy devices is mainly related to the cost of the cathodic ORR electrocatalyst. Hence, a cost-effective and environmentally benign approach is highly demanding to design the electrocatalyst for ORR and replacing noble metal-based electrocatalyst. In this regard, biomass-derived hierarchically porous carbon-based materials have become attractive options compared to metal-based electrocatalysts due to their several advantages such as abundance in nature, economic viability, characteristic sustainability, environmental friendliness, and excellent physicochemical properties. Moreover, harsh chemicals are not being involved during their synthesis, and they intrinsically possess a variety of heteroatoms (N, P, S, etc.), which are key for augmenting the electrocatalytic activity. In the present review article, the recent progress on biomass-derived cathode electrocatalysts has been summarized for ORR including a brief account of bioresource selection, synthesis methods, and processing criteria that greatly influences the electrocatalytic activity.

Keywords: biomass; pyrolysis; porous carbon; heteroatom doping; electrocatalysts; oxygen reduction reaction; fuel cell

Citation: Das, S.; Ghosh, S.; Kuila, T.; Murmu, N.C.; Kundu, A. Biomass-Derived Advanced Carbon-Based Electrocatalysts for Oxygen Reduction Reaction. *Biomass* **2022**, 2, 155–177. https://doi.org/10.3390/biomass2030010

Academic Editor: Giorgos Markou

Received: 14 July 2022
Accepted: 11 August 2022
Published: 15 August 2022

1. Introduction

The rapidly increasing concerns regarding exhaustion of fossil fuel and environmental deterioration have gathered global awareness for renewable energy production to develop sustainable society. Recently, various electrochemical technologies are being adopted to execute the reduction of climate change, and environmental pollution. For example, fuel cells (FC), metal-air batteries (MABs), water electrolyzers, etc., have been regarded as dependable as well as clean, eco-friendly, and affordable energy storage/conversion devices [1]. The performance and efficiency of many energy conversions and storage systems are mainly governed by oxygen reduction reaction (ORR) which was firstly reported by Jasinski in 1964 using co-phthalocyanine as a precursor [2]. However, the ORR process is kinetically sluggish requiring high overpotential and hence, robust electrocatalysts are often required to trigger the ORR process. Until now, Pt-based materials are considered as the benchmark electrocatalysts for ORR in terms of achieving high positive onset potential, half-wave potential, and high limiting current density. Nonetheless, high cost, scarcity, and poor durability are the main constraints from make them industrially viable.

Recently, the main aim of the researchers is to substitute Pt-based materials with cost-effective, efficient, and stable non-precious metal-based/metal-free materials. To achieve this goal, a library of platinum group metal (PGM) free electrocatalysts have been developed which can be divided into two branches: non-precious transition metal-based

electrocatalysts including metal-coordinated nitrogen-doped carbon (M−N−C) [3–5], transition metal-based oxides [6], transition metal nitrides [7], phosphides [8], perovskites [9], transition metal chalcogenides [10], and heteroatom or multi atom doped carbon-based materials [11]. Although many electrocatalysts showed promising electrocatalytic activity toward ORR rivaling state-of-the-art Pt/C but there is plenty of room to improve the stability of these transition metal-based electrocatalysts to be considered for commercial uses.

Metal-free carbon-based materials have become a promising alternative to transition metals due to their organized electrical conductivity, durability, stability, tunable surface morphology, and adjustable (micro, meso, macro) porous structure. Moreover, the doping of heteroatom (N, P, S, B, etc.) in the sp^2 carbon template can alter the electronic distribution over carbon owing to the generated electronegativity difference [3]. As a consequence, this will help to facilitate oxygen adsorption as well as the breaking of O-O bond rather than pristine carbon. It is important to mention that the advent of carbon nanotubes (CNTs) and graphene have profoundly encouraged the development of carbon-based electrodes for ORR. In spite of the promising performance of CNT or graphene-based materials in ORR, their utilization on a large scale is hindered by the high synthetic costs. Hence, highly earth-abundant biomass resources have garnered attention as sustainable and alternative option to design carbon-based materials for green energy storage devices due to their low cost, and inherent presence of heteroatoms.

The main resources of biomass are carbohydrates, polysaccharides, lignocellulose biomass, animal-based biomass, human waste-based biomass, etc. which are globally produced as waste in tons every single day [12]. These wastes pose a great challenge to waste management and this can be regarded as a potential option to convert the waste to novel carbon-based materials for versatile electrochemical applications. Indeed, the conversion of biomass to electrode materials for energy and environmental applications gained huge attention and has been highlighted recently [13–15]. Cellulose, hemicellulose, and lignin's are the primary configurational components of biomass [12].

Pristine biomass-derived carbon is not useful as electrode material. So, activation of biomass is required which can be accomplished by tuning the porosity, surface area, and binding capability. This can be achieved either through the physical activation or chemical activation method [3,16]. For industrial purposes, activated carbon is produced from biomass via the dual-step physical activation method followed by gasification at high temperatures (600–1000 °C). The number of developed porosities is directly proportional to the number of carbon atoms present. The production of carbon monoxide gas during gasification leads to the formation of pores. However, the size and shape of pores completely depend upon the reaction conditions. On the other hand, in chemical activation, a one-step process is used for lab-scale synthesis followed by thermal treatment and impregnation of dehydrating chemicals for example KOH, NaOH, $ZnCl_2$, H_3PO_4, etc. There are advantages as well as disadvantages to both methods. For example, in the physical activation method, the polarity of the biochar surface, as well as oxygen containing functional groups, can be increased but it requires very high temperature, and it is hard to control the porosity. In contrast, the porosity can be controlled by suitable impregnation ratio, activation duration, and temperature by utilizing the chemical activation method, but this is time and energy consuming involving costly chemicals. Hence, the physical and chemical activation method can be rationally combined to obtain the desired property and it is suggested for delicate tailoring of porosity [17]. Apart from that template method is widely used to control the porosity which includes hard templates, soft templates, and dual templates. At present, various kinds of biomass precursors are used to obtain activated carbon for the ORR and other energy-based applications [18–23]. In the present review article, instead of focusing on the synthesis protocols of biomass-derived carbon nanomaterials, an overview of advancements in biomass-derived electrocatalysts for the ORR is provided along with a short account of the ORR mechanism.

2. Fundamentals of ORR

ORR has been the subject of huge investigation over the decades (Figure 1a) since it is at the heart of various energy conversion and storage systems such as fuel cells, metal-air batteries, and so on [24,25]. Among all the studied catalysts, Pt is the state-of-the-art catalyst for ORR due to its moderate affinity to the reactive intermediate species formed on the surface of an electrode during the course of the reaction. Moreover, Pt possesses the highest electrochemical activity towards ORR owing to its appropriate d–band vacancy (0.6 per atom), and reasonable oxygen adsorption capability [26]. Until now, various mechanism for ORR has been put forward, however; it can follow either dissociative or associative one (Figure 1b).

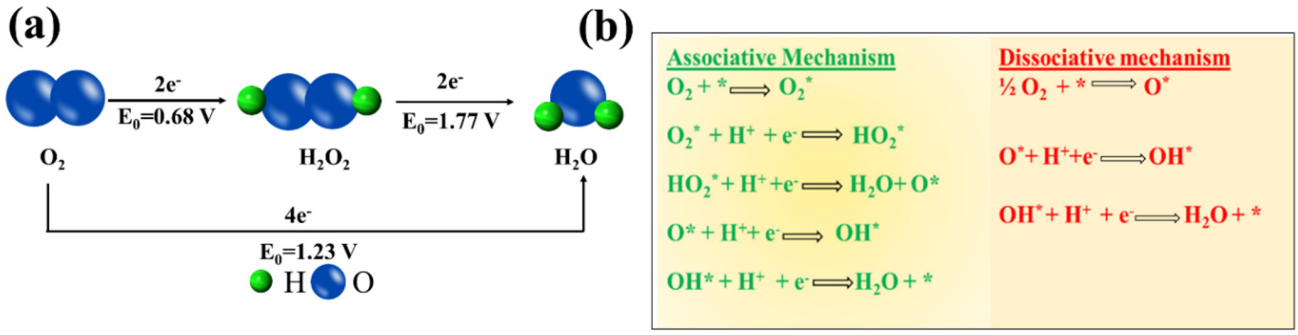

Figure 1. (**a**) Scheme of the ORR mechanism by direct pathway and indirect pathway, (**b**) ORR mechanism on the catalyst surface (* notation denotes a site on the catalyst surface).

The mechanistic pathway is governed not only by the oxygen adsorption mode, but it also depends on the dissociation barrier of the catalyst surface [27]. The adsorption of O_2 over the active site of the catalyst is mainly of two types: bidentate O_2 adsorption (Yeager model) and end-on or monodentate O_2 adsorption (Figure S1) [28]. The first one leads to the direct four-electron pathway resulting in H_2O as the product whereas the second one follows a two-electron pathway with peroxide formation, respectively [29,30].

It is noteworthy to mention that for practical applications like fuel cells, metal-air batteries, etc., the four-electron pathway is a more desired one since the formation of peroxide species can be avoided which caters to the degradation of the catalyst. The formation of highly reactive oxygen intermediates in ORR such as OOH*, OH*, O* (* denotes a site on the catalyst surface) is associated with the involvement of a complicated multi-step electron transfer process. The electrocatalytic activity is largely determined by the binding energies of the reactive oxygen species to the catalyst surface. Hence, to design highly active materials it is a prerequisite to have knowledge of how to control the binding energies of reactive intermediates on a catalyst surface. On the basis of density functional theory calculations, Nørskov and his group have calculated the free energies of the surface intermediates for a series of metals [27]. This group has also established a trend in thermodynamic limitations for the metals and constructed a volcano-shaped plot that relates the theoretical ORR activity and oxygen adsorption energy. The model indicates that Pt sits near the top and explains why Pt is regarded as the best cathode material. However, it is important to note that Pt is not situated at the "summit of the volcano" (Figure S2) and hence alloying with 3d transition metals can be used to improve its performance [31].

2.1. Basic Parameters to Evaluate ORR Catalysts

After Levich's seminal discovery of the rotating disk electrode (RDE) in 1944, it is widely used to study the ORR kinetics from the polarization curve [32]. The polarization curve is generally divided into three well-defined regions namely kinetic, mixed (kinetic + diffusion), and diffusion-limited zone and in each part, the ORR kinetics are controlled in different ways. Apart from that, some widely accepted parameters such as the onset potential (E_{onset}), half-wave potential ($E_{1/2}$), and diffusion-limited current density (J_L) can be deduced from the polarization curve for apprising the electrochemical activity

of the investigated electrocatalyst. These parameters will be defined later but it is necessary to highlight that the more positive the E_{onset}, $E_{1/2}$, and high J_L values, the more active the electrocatalyst for ORR. In the kinetic-controlled area, the ORR reaction is sluggish, and the current density increases to some extent as the potential decreases (Figure S3). In a mixed (kinetic and diffusion-controlled zone) region, the reaction accelerates as the potential drops and a remarkable increase in the current density can be observed. In this particular region, the current density is inversely proportional to the applied potential. In the diffusion-controlled zone (plateau region of the curve), the current density can be precisely determined by convection, and it reaches a platform at a certain rotating speed.

2.1.1. Onset Potential and Half-Wave Potential

The definitions of the E_{onset} vary a lot in literature and the experimental determination is also quite arbitrary. However, onset potential usually refers to the potential when the current diverges from the baseline and the most common approach is to find the intersection of the tangents between the baseline and the increasing current in the polarization curve (Figure S3). Apart from that, the potential corresponding to 5% of the J_L and the potential at which the ORR current density does not exceed a value of 0.1 mA cm^{-2} were also proposed to define the onset potential [33]. $E_{1/2}$ is another basic parameter, and it is directly calculated from the midpoint of obtained LSV curve at 1600 rpm. It is basically the potential corresponding to half of the diffusion limiting current density.

2.1.2. Kinetic Current Density

Kinetic current density (J_k) is one of the important parameters to determine the catalytic activity of an ORR catalyst. Mass transport corrected polarization curve predicts the value of J_k and can be obtained with the help of Koutecky-Levich (K-L) equation:

$$1/J = 1/J_k + 1/J_L$$

To minimize the error in mass transport correction, different catalysts are compared with respect to kinetic current density at a higher potential region.

2.1.3. Electron Transfer Number and HO_2^- Percentage

The number of electron transfer (n) and the percentage of HO_2^- intermediate are also basic parameters to understand ORR kinetics. These parameters can be determined from RDE or RRDE (rotating ring disk electrode) techniques which are effective for investigating the kinetics of multistep charge transfer reactions. K-L equation is generally utilized to calculate the "n" value and obtained by plotting ($1/J_L$) against the square root of rotation rate ($\omega^{-1/2}$), which is widely known as the K-L plot.

For

$$\text{RDE, } J_L = B\omega^{1/2}$$

where

$$B = 0.62\, nFC_0\, (D_0)^{2/3}\, \nu^{-1/6}$$

where, ω is the electrode rotating rate (rad s^{-1}), n is the number of electrons, F is the Faraday constant (F = 96485 C mol^{-1}), C_0 ($C_0 = 1.2 \times 10^{-6}$ mol cm^{-3}) and D_0 ($D_0 = 1.9 \times 10^{-5}$ cm^2 s^{-1}) denotes the concentration and diffusion coefficients of O_2 in 0.1 M KOH, respectively, υ is the kinematic viscosity of the electrolyte (0.01 cm^2 s^{-1}), and k is the electron transfer rate constant [34]. The "n" value can also be calculated from the RRDE technique by using the following equation:

$$4J_D = n\,(J_D + J_R/N)$$

where J_D is the disc current density, J_R is the ring current density, and N is the RRDE collection efficiency, *n* is the number of electron transfers during the reaction. The percentage of intermediate species for ORR is calculated by the equation given below:

$$\% HO_2^- = 200J_R/(NJ_D + J_R)$$

3. Strategies for Enhancing the ORR Activity of Biomass-Derived Carbonaceous Material

Several strategies are being adopted to synthesize and trigger the ORR activity of biomass-derived carbon-based nanomaterials. Among them, heteroatom doping to modulate the sp^2 carbon and modulation of porosity via different activation methods are largely utilized. In the following section, factors that are very important to control the ORR activity have been discussed thoroughly.

3.1. Modulation of sp^2 Carbon via Monoheteroatom/Multiheteroatom Doping for ORR

Due to the reluctant nature of pristine carbon towards the adsorption of ORR intermediates, some structural modification/modulation is necessary to fabricate ORR active sp^2 carbon matrix. Heteroatom doping, intermolecular charge transfer, and generation of structural defects are the three well-established strategies to make ORR active carbon matrix from pristine sp^2 carbon [35]. Among these strategies, heteroatom doping is the most promising and convenient one in very recent time. The factors which are responsible to enhance ORR activity after the incorporation of heteroatom are (i) disturbance in electroneutrality, (ii) alteration in spin density, (iii) charge redistribution, (iv) binding states, and (v) tunable pore sizes and lengths. The first four refinements tune the adsorption ability of ORR intermediates which further facilitates the direct reduction of oxygen via a $4e^-$ mechanism with a low % of H_2O_2 formation and the last one controls the mass transfer during the reaction progress. These factors play a key role in triggering the ORR activity of the pristine carbon matrix. Different kinds of N-atom, such as pyrrolic-N, pyridinic-N, graphitic-N, and quaternary-N, present in the carbon matrix determine the activity parameter for ORR. The actual role of the different types of nitrogen that are doped into the carbon matrix is still a debatable research topic. However, among all types of nitrogen atom graphitic-N plays an important role in enhancing the J_L value, and pyridinic-N reduces the overpotential value for ORR, which are very important in deciding catalytic activity for any ORR active catalyst [36]. Depending upon activity different types of nitrogen follow the trend as pyridinic-N > pyrrolic-N > graphitic-N > oxidized-N > carbon (Figure S4). Nonetheless, the presence of this different nitrogen can be assigned by X-ray photoelectron spectroscopy (XPS) through the deconvolution of the N 1S peak but the actual activity and role of these N-atoms should be critically reviewed for understanding the real mechanism [37]. Along with nitrogen other non-metal elements (B, F, S, P, etc.) have been successfully inserted into the carbon matrix to generate multidoped sp2 carbon matrix which can provide moderate binding affinity toward ORR intermediates (Figure S5). Multi-heteroatom doping is an efficient and rational way to form a hierarchical porous structure through which rapid charge transfer and enlargement in spin density on the adjacent carbon atoms take place during the reaction course [38,39].

3.2. Modulation of Porosity

Sluggish ORR reaction generally required three-phase interaction of catalyst layer (solid), electrolyte (liquid), and O_2 diffusion from the air (gas). So, the hierarchical pores and length of the pore channels through which electrolyte and gas can be transferred, are crucial parameters for catalytic performance. The length of pore channels is inversely proportional to ORR electrocatalytic activity [40]. This is because lower resistance and high charge transfer take place when the channel length is decreased compared to the longer one. Besides, with increasing the pore size the electrocatalytic activity also increases, and as a consequence, mesoporous (2 nm to 50 nm pore size) materials show excellent catalytic

performance compared to microporous (less than 2 nm Pore size) materials. This can be ascribed to the interconnected mesoporous criss-cross network which influences mass transfer due to decreased and smooth diffusion pathways [40]. Generally ordered mesoporous carbons are less common in which a hierarchical array of micro, meso, and macro pores are present than the non-ordered mesoporous ones. This non-ordered mesoporous carbon can form plenty of porous nanomaterials. These non-ordered carbon nanomaterials can show excellent and comparable performance to that of ordered mesoporous carbon materials due to the existence of micropores which are present within nanoscale ion transport distance from the neighboring mesopores and macropores. Along with tunable porosity, the introduction of heteroatom via doping promotes electrocatalytic performance due to charge alteration and spin density modification [41]. The hydrothermal carbonization (HTC) technique is a very effective and safe approach for the conversion of biomass to value-added materials (bio-alcohols, bio-char, gaseous bio-fuels). The processes involved in the mechanism of HTC are decarboxylation, condensation, dehydration, polymerization, hydrolysis, and aromatization. However, numerous factors, including temperature, duration of the reaction, pressure, the type of catalyst employed, and the biomass to-water ratio, affect the quality of the resulting yield produced by the HTC process [17]. Further activation and graphitization are required because HTC-derived carbons typically have low surface areas (<10 m^2 g^{-1}) and poor electron conductivity [1]. However, the HTC process of biomass has a significant drawback because it generates a lot of wastewater and liquid oil, both of which have not yet been resolved. So, it is imperative to comment that activation is of utmost necessity to modulate the shape and mesopores/micropores ratio. The activation process can be further classified into different methods depending on their mechanism which are physical activation, chemical activation, dual (physical and chemical) activation, self-activation, template activation, etc. [17]. In this section, some frequently used optimization techniques are discussed in a nutshell.

3.2.1. Physical Activation

To ensure the porosity of biomass-derived materials physical activation is largely utilized since it is a very cheap activation method. In between 600–1000 °C temperature and atmospheric pressure, new pores are obtained by gasification in presence of steam, N_2, O_2, and CO_2 by kicking out the carbon atoms selectively [17]. In some cases, blockage of blocked pores is cleared by the gasification method. During the gasification, CO_2/steam reacts with biomass-derived carbon to generate gasses for example CO, H_2, and CH_4. Moreover, the amount of the released gases is directly proportional to the number of pores generated. The main focus of the physical activation is described below briefly in a nutshell: (i) creation of new pores, (ii) opening of previously blocked pores, (iii) broadening of pores. Nonetheless, there are some parameters such as temperature, time, and CO_2 flow rate on which activation, surface area, and porous nature are dependent. An increase in activation temperature leads to the formation of pores, tuning of the size of pores, and enhancement in the mesopores/micropores ratio [42,43]. Activation time also affects the formation of micropores and mesopores, which is extensively time-dependent and will collapse after a long time of activation. A higher CO_2 flow rate results in carbon burnout, which is not acceptable for hierarchical pore formation [44,45]. Fu et al. successfully prepared porous graphitic carbon nitride/ carbon (g–CN/C–2) composite through high-temperature treatment at 600 °C using glucose as the carbon source and melamine, and cyanuric acid as graphitic carbon nitride precursor (Figure 2a) [46]. The synthesized material consists of a 3D interconnected carbon matrix and porous structure. The porous morphology with a large surface area of 450 m^2 g^{-1} could be helpful in achieving higher catalytic activity (Figure 2b). The electrocatalytic activity of the as-prepared catalyst was obtained with an E_{onset} of 0.90 V vs. RHE, $E_{1/2}$ of 0.79 V vs. RHE, limiting current density (J_L) = 4.10 mA cm^{-2} and 3.4–3.5 of transferred electrons (n) in 0.1 M KOH and low charge transfer resistance (Figure 2c–e). A higher n value and lower charge transfer resistance manifests promising catalytic performance with enhanced catalytic activity.

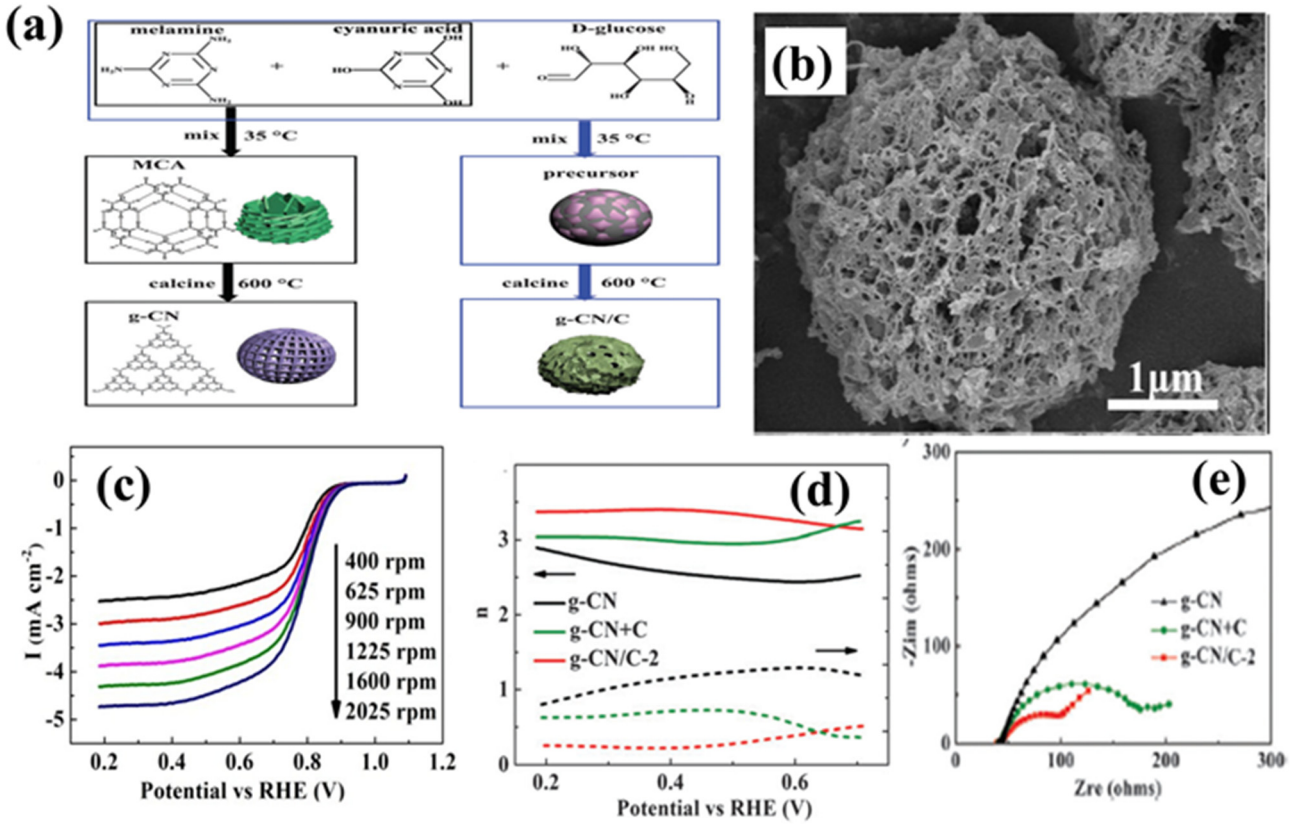

Figure 2. (**a**) Schematic illustration of the synthesis of g–CN and g–CN/C, (**b**) SEM images of g–CN/C–2, (**c**) LSV polarization curve for ORR, (**d**) evaluation of *n* value, (**e**) EIS studies of the g–CN/C–2, g–CN + C, g–CN, adapted from [46].

3.2.2. Chemical Activation

The chemical activation process is a hybrid process in which the mixing of biomass with activating agent occurs followed by thermal treatment at a desirable temperature. In this one-step method acid, strong base, or salt are used during chemical activation to enhance the porosity. Generally, chemicals such as KOH, $ZnCl_2$, ZnO, H_3PO_4, etc. are introduced [47]. Though the activation mechanism of KOH is very complex, it is quite promising due to the requirement of low activation temperature, high amount of product yield, and hierarchical micropores arrangement. Three possible mechanisms have been ascribed (Figure 3) [48,49]: (i) during thermal treatment/calcination K_2CO_3, K_2O formed along with KOH, resulting in the formation of nanopores, (ii) at high-temperature intermediate products such as CO_2, and H_2O are vaporized via the gasification method leaving pores into the carbon matrix, and (iii) generated metallic K intercalates into the carbon lattices resulting in the exfoliation of carbon layers, which directly increases the porosity. Besides that, $ZnCl_2$ is also used as an activating agent [50]. Due to its Lewis acid characteristics, $ZnCl_2$ enhance the dehydration and condensation reaction at both low and high temperature.

Recently by using glucose as a carbon source and dicyandiamide (DCDA) as a nitrogen source Liu et al. have developed a facile hydrothermal method to produce N-doped carbon spheres (THNC) [51]. After that chemical activation was done by $ZnCl_2$ along with thermal treatment between 700 to 900 °C. Among these annealed products, THNC-800 exhibits superior catalytic performance due to the formation of highly N-doped porous carbon (Figure 4a). It is ascribed that $ZnCl_2$ not only acts as a structural template but also facilitates the formation of a porous network with a large surface area of 1036.1 $m^2\ g^{-1}$ and a large pore volume of 0.53 $cm^3 g^{-1}$. The electrocatalytic performance of the as-prepared catalyst was obtained with an E_{onset} = 0.92 V vs RHE, limiting current density J_L = 3.0mA cm^{-2}

(Figure 4b), and *n* values in the range of 3.5–3.9 of (Figure 4c) in alkaline medium. The high electrocatalytic activity, as well as durability, might be the consequence of highly doped pyridinic and graphitic nitrogen content in the carbon matrix (Figure 4d) Furthermore, uniformly distributed mesoporous structure enhances the mass transfer during the course of the reaction.

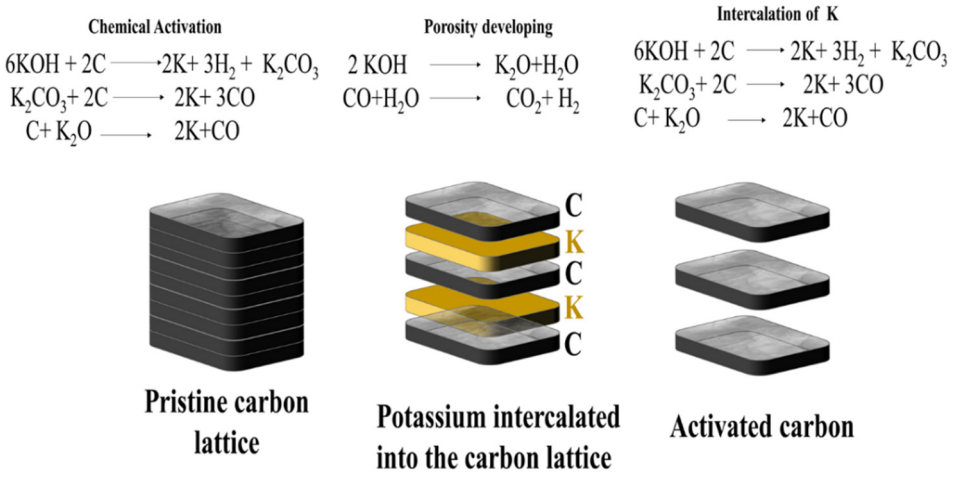

Figure 3. Activation mechanism by the intercalation of metallic K into the pristine carbon lattices, the expansion of the lattices by the intercalated metallic K, and the removal of the intercalated K from the carbon matrix adapted from [49].

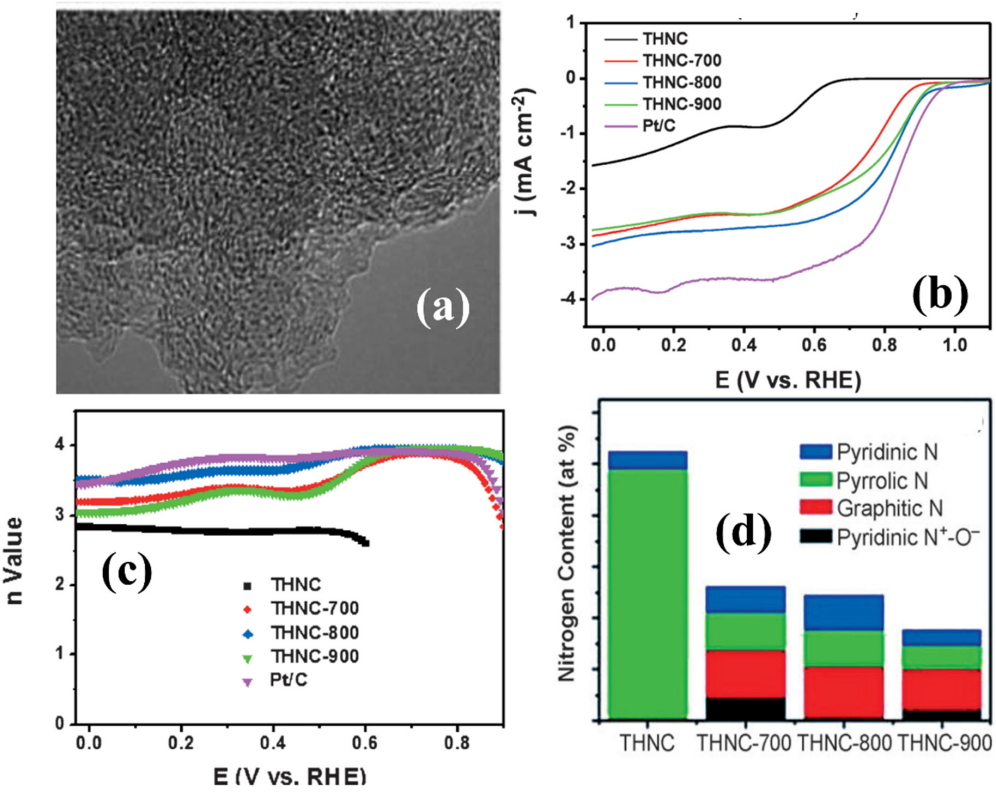

Figure 4. (**a**) TEM image of THNC-800, (**b**) RRDE voltammograms of the same electrodes at the rotation rate of 1600 rpm. Scan rate: 10 mVs^{-1}, (**c**) variation of *n* values of THNC, THNC-700, THNC-800, THNC-900, and Pt/C at different potentials, (**d**) graphical representation of the nitrogen content in the carbon samples, adapted from [51].

3.2.3. Self-Activation

In the case of self-activation, additional activating agents are not required which is economically and environmentally more viable [52]. Adsorbed oxygen by the raw biomass material and the air present in the sealed reactor vessel contribute as an activating agent [53]. Physical self-activation and chemical self-activation processes are two main processes that happen in the self-activation. In the physical activation process, the released gas from biomass precursors is utilized for the activation of carbon [54]. Whereas in the chemical self-activation process the existing inorganic compound in the biomass contributes to the activation of carbon [55]. Presently Wang et al. have prepared N-doped porous carbon from fish bones followed by a double pyrolysis method at 800 °C [52]. The as-prepared catalyst shows decent catalytic performance towards ORR with a number of transferred electrons ranging from 3.5 to 3.6.

(Figure 5a,b) at 1600 rpm. The exhibited catalytic performance can be ascribed due to the high surface area (563 m^2g^{-1}), uniformly distributed mesopores along with a large number of micropores (Figure 5c), and the presence of pyridinic and quaternary nitrogen atoms (Figure 5d).

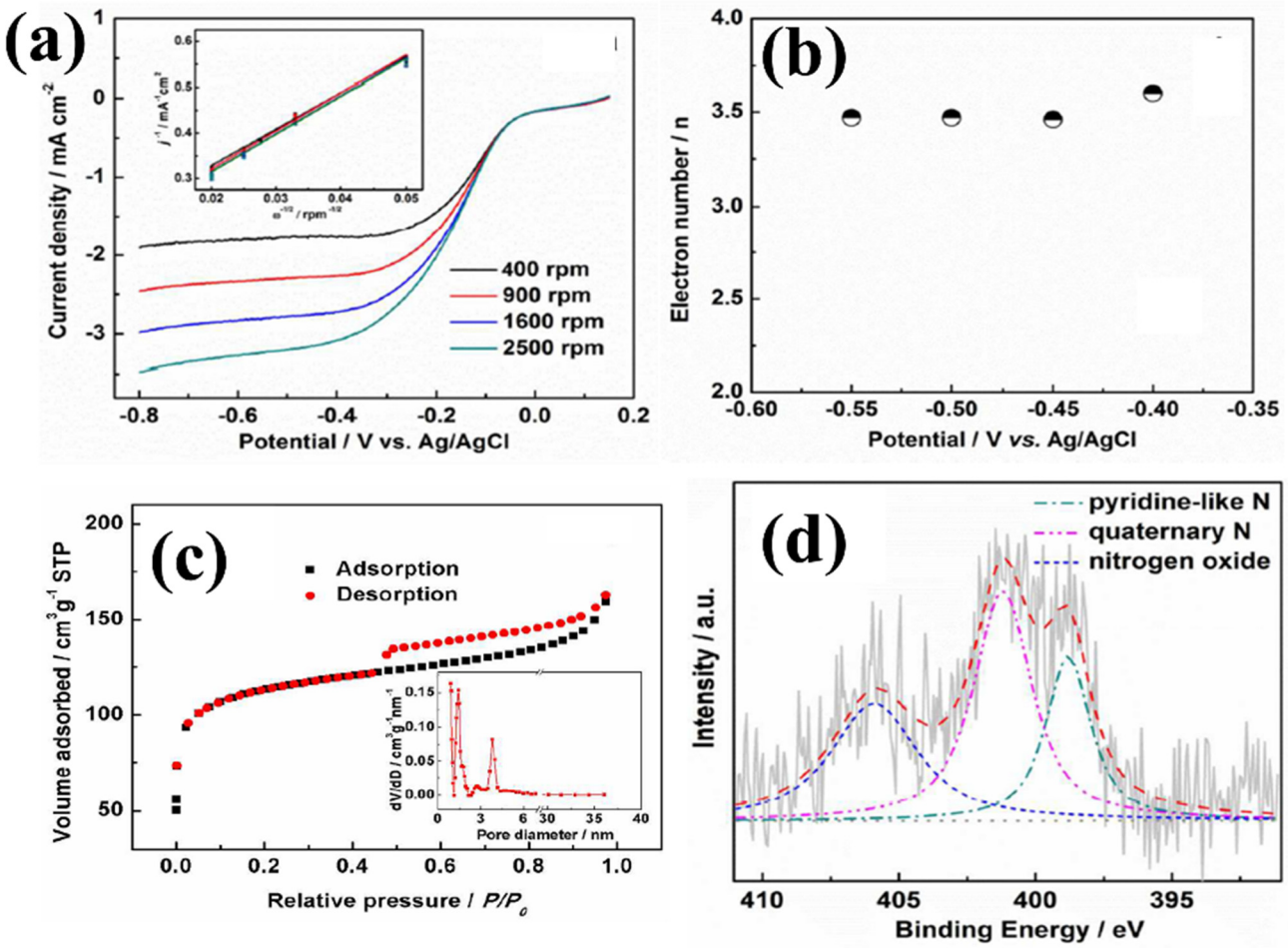

Figure 5. (**a**) LSVs for ORR in O_2–saturated 0.1 mol L^{-1} KOH solution on CFB at various rotation rates, scan rate 5 mV s^{-1}; (Inset: the corresponding K–L plots for ORR), (**b**) the number of transferred electrons at a different potential, (**c**) N_2 adsorption-desorption isotherms of CFB (Inset shows the corresponding pore size distribution), (**d**) High–resolution XPS spectrum at N1s region of CFB, adapted from [52].

3.2.4. Template Activation

It is challenging to uniformly tune the pore size as well as pore distribution for both physical and chemical activation processes. Template activation can be used to create

porous nanostructures with a consistent layout and variable pore size. The key advantage of this methodology is that a template can be fabricated based on the specifications of synthetic material, size, and form. The nature of the template determines whether it is a hard template or a soft template [13].

Hard Template Method

Stuffing monomers into the template by chemical reaction is known as the hard template method because by removing the template porous material is obtained. SiO_2 is most widely used as a hard template to produce porous carbonaceous materials. Using hard templates is a very time taking and expensive method for industrial application. Besides it, hazardous inorganic materials such as HF, and NaOH are used which are very harsh to the environment [17]. Lin et al. demonstrated the ORR performance of soybean-derived nitrogen-doped hierarchical micro-mesoporous carbon via hard templating carbonization method with subsequent KOH activation (Figure 6a) [56]. The as-prepared activated nitrogen-doped porous carbon (ANPC–3 with KOH: carbon mass ratio = 3:1) boost the ORR performance compared to other counterparts. It is ascribed that silica templating followed by KOH treatment leads to the formation of micro- mesoporous texture with a specific surface area of 1749 m^2 g^{-1} (Figure 6b,c). Furthermore, a combination of micro and mesopores serves as the reservoir of alkaline electrolytes that can trigger the diffusion of ions as well as mass transfer. Likewise, ANPC–3 showed enhanced catalytic activity in terms of more positive half-wave potential (0.79 V vs. RHE), high limiting current density (5.09 $mAcm^{-2}$ at 0.23V vs. RHE), and methanol tolerance compared to other catalysts having different KOH/carbon mass ratio (Figure 6d).

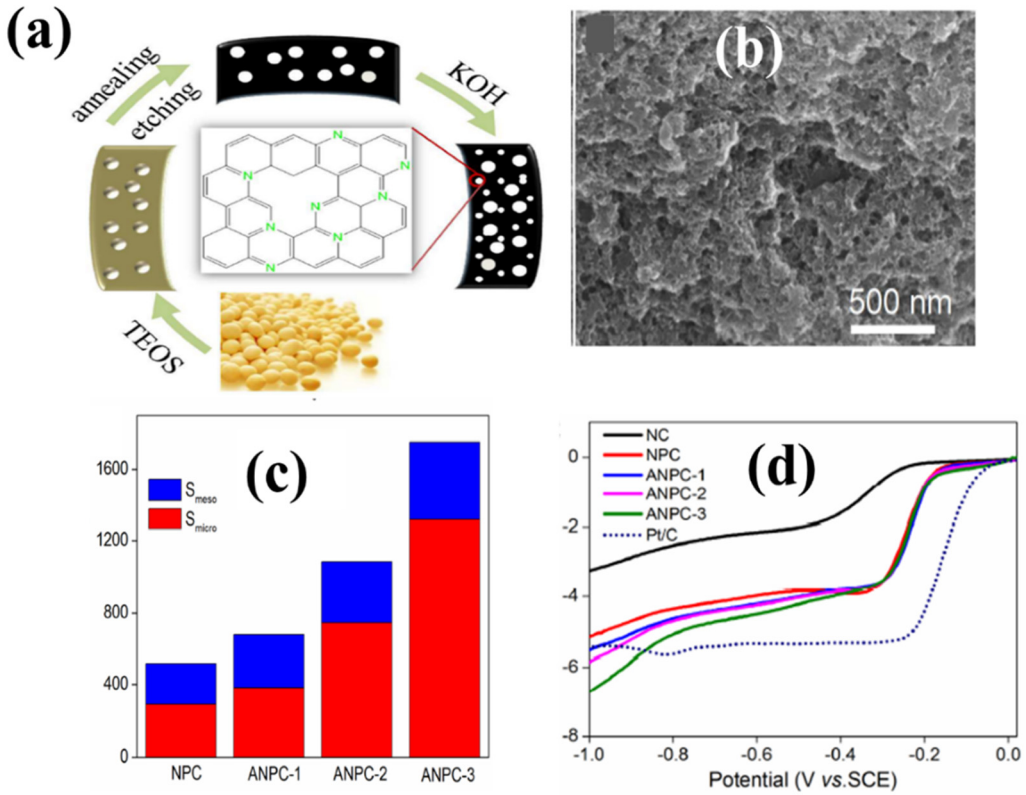

Figure 6. (**a**) Synthesis procedure diagram, (**b**) SEM image of ANPC–3, (**c**) the surface area values in the range of mesopores and micropores, (**d**) LSV curves of samples at 1600 rpm, adapted from [56].

Soft Template Method

The urge of removing harsh chemicals used in the hard template method has forced the researchers to focus on an alternate simpler soft template method. Amphiphilic molecules such as block co-polymers and surfactants assist ordered aggregates which are used as the

template in the soft-template method [57]. The soft-template approach is typically used to create mesopores. However, soft templates are unable to create materials with high activity and stability due to low molecular weight, poor durability, and single composition [58]. Wu et al. have prepared phosphorus-doped carbon hollow spheres (P–CHS) by using anionic surfactant sodium dodecyl sulfate as a soft template (Figure 7a) [59]. The as-prepared P–CHS has a large surface area of 654.4 m^2 g^{-1} with 0.36 cm^3 g^{-1} pore volume. The authors showed that the catalyst exhibits ORR catalytic performance with E_{onset} = 0.89 V vs. RHE, J_L = 5.6 mA cm^{-2}. The *n* value, 3.86 suggests that the ORR process is following $4e^-$ pathway (Figure 7b,c). This result indicates that P doping promotes ORR activity. This method opens up the possibilities of heteroatom doped carbon hollow sphere formation in via a facile strategy. The dual template method is also a well-accepted method to produce porous carbon material for oxygen reduction reaction [60].

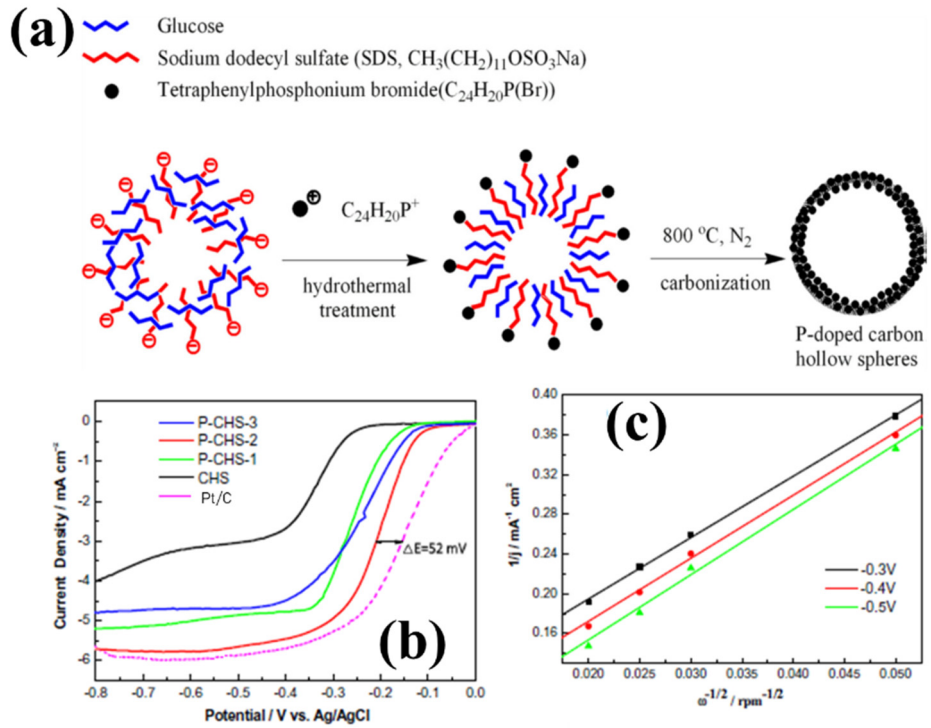

Figure 7. (**a**) Schematic illustration of the preparation of P–doped carbon hollow spheres, (**b**) linear sweeping voltammograms of the ORR on the samples with a rotating speed of 1600 rpm, (**c**) the K–L plots of ORR on PCHS–2 at different electrode rotating speeds, adapted from [59].

4. Biomass-Derived Carbon-Based Materials for ORR

4.1. Carbohydrates and Polysaccharides

Polyhydroxy aldehydes or ketones made of carbon, hydrogen, and oxygen are referred to as carbohydrates. Because of their ability to significantly improve ORR, carbohydrates have recently attracted both academic and commercial attention. Glucose can currently be purchased for ten times less than the precursors that contain heteroatoms, such as ferrocene, vitamin B_{12}, etc. As a consequence, glucose is frequently employed as a precursor for designing porous hollow carbon structures by various activation processes and synthesis techniques. Here, in this section recent research on the use of glucose as a precursor for metal-free biomass-derived ORR catalysts has been reviewed [46,61–69]. Li and co-workers revealed that simultaneous doping of nitrogen and sulfur into the mesoporous carbon network derived from glucose may substantially modify the ORR functionality [61]. Using mesoporous SBA–15 as a silica template and ammonia, thiophene as the N, and S dopant, they synthesized N–S–CMK–3, which was subsequently pyrolyzed at a high temperature (Figure 8a). The designed material possesses a huge surface area of 1023 m^2 g^{-1} with a homogeneous structure that includes mesopores and macropores (Figure 8b). The as-

synthesized catalyst showed superior catalytic activity with E_{onset} = 0.92 V vs. RHE, $E_{1/2}$ = 0.73 V vs. RHE, and J_L = 5.50 mA cm^{-2}, and n = 3.96 which indicates that the oxygen reduction follows the $4e^-$ path (Figure 8c,d). The extra sulfur atom doping of N-S–CMK–3, which further increases the positive charge and asymmetric spin density of nearby carbon atoms, may be responsible for its high catalytic activity. Ma and co-workers synthesized N–doped mesoporous carbon nanosheet /carbon nanotube (N–MCN/CNT) hybrids which exhibited tremendous ORR activity and durability [62]. The CNTs' aqueous solution was quickly mixed with glucose and urea before being exposed to an inert gas for annealing (Figure 9a). The hybrid catalyst shows excellent ORR activity (Figure 9b,c). A limited amount of H_2O_2 generation and a high n value (3.9) indicate that the ORR process follows the 4-electron route. According to the authors, CNTs are essential not only for quick electron transfer but also for promoting mass transport diffusion via channels and active site surface areas. Employing a facile hydrothermal process and pyrolysis in the NH_3 atmosphere, a low-cost, straightforward, and environmentally friendly method for the creation of self-doped nitrogen porous carbon materials from spirulina has been developed by Liu et al. [63]. The as-prepared catalyst shows remarkable catalytic activity with E_{onset} = 0.99 V vs. RHE, $E_{1/2}$ = 0.87 V vs. RHE, J_L = 5.8 mA cm^{-2} along with n = 4, suggesting facile kinetics for the ORR process. The high activity can be attributed to the enormous specific surface area with dense mesoporous structures, as well as the high pyridinic nitrogen and low oxidized nitrogen percentages. A series of N–doped oxygen-containing nitrogen-doped carbon (ONC) nanosheets with large surface-active site area and high porosity were synthesized by in situ formed g-C_3N_4 templates [64]. ONC– 560 exhibited good tolerance to methanol as well as good long-term durability. The as-prepared catalyst has a surface area of 610 m^2 g^{-1}, an E_{onset} = 0.95 V versus RHE, an $E_{1/2}$ = 0.81 V vs. RHE, and a J_L = 5.7 mA cm^{-2}. The amount of electron transfers also indicates that the reaction follows the $4e^-$ route. Cost-effective ONC materials prepared by this strategy could pave the way to developing excellent carbon-based electrocatalysts. Zheng and co-workers have developed a novel form of N-doped carbon tubes (NCTs) that exhibit excellent electrocatalytic ORR activities [65]. Further development of the novel hierarchical carbon structure and optimization of nitrogen doping is needed to address the issues of ORR activity of different catalysts. Excellent ORR catalytic activity is caused by a significant series of tiny nanotubes that have developed on the surface of the hierarchical structure. Authors have suggested that pyridinic and graphitic nitrogen are the majorly contributing active sites. Due to the challenges in properly synthesizing the form of N dopant in carbon materials generated from biomass, the origin of the catalytic mechanism underlying the activity of N-doped carbon electrocatalysts for ORR is still unknown. Ryoo and co-workers developed ordered mesoporous carbon (OMC) for the first time, utilizing sucrose as a carbon source and mesoporous silica as a hard template [70]. Since then, researchers have promoted the use of sucrose as a starting material for many types of synthesis [71–73]. Sun et al. suggested a template-free technique to create S-doped carbon spheres using sucrose. In alkaline media, an increase in ORR activity was shown to be caused by the presence of S atoms [72]. A swelling-induced method was introduced for the pyrolysis of porous sucrose-derived spheres (PSS) in the presence of DCDA to create N-doped graphene (NG) (Figure 10a) [73]. PSS is primarily used as a carbon framework precursor in this synthesis, which also helps in shaping two-dimensional (2D) crumpled NG under the swelling force from the heat condensation of DCDA. It is suggested that the unique 2D carbon nanomaterials can be fabricated using the suggested chemical method. Moreover, TEM images revealed that NG–1000 comprises twisted and interconnected flake-like layers, and it is made up of a few layers of bent graphene with an interlayer gap of approximately 0.34 nm (Figure 10b,c). The as-prepared catalyst NG–1000 imparts good catalytic activity with E_{onset} = 0.90 V vs. RHE, $E_{1/2}$ = 0.79 V vs. RHE, J_L= 4.3 mA cm^{-2} and n = 3.9. These electrochemical parameters reflect that the catalyst adopts a $4e^-$ mechanism (Figure 10d–f). It is ascribed that the combination of the high proportion of graphitic nitrogen and the ideal total nitrogen concentration results in ultrahigh ORR activity for NG. This method resulted

in a decrease in N content, from 8.7 to 2.6%, while enhancing ORR activity because of a higher degree of graphitization. However, raising the pyrolysis temperature from 800 to 1100 °C had no effect on the graphene morphology.

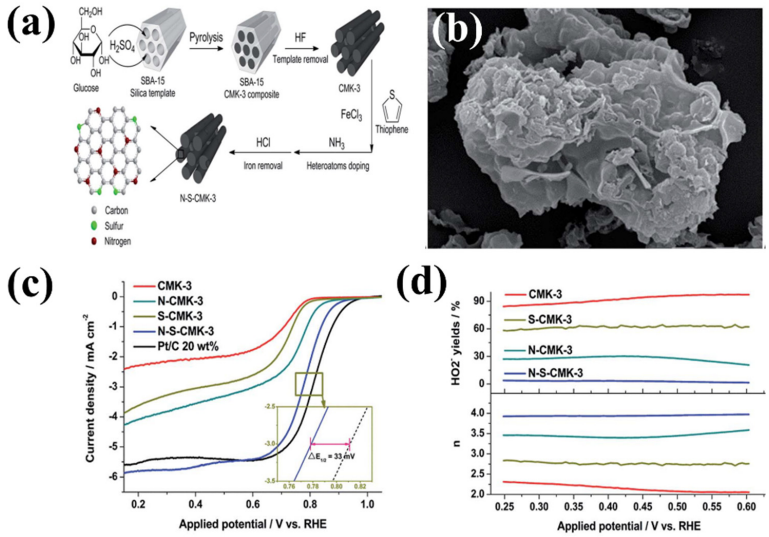

Figure 8. (**a**) Schematic of the synthesis of metal-free mesoporous N–S–CMK-3 catalysts, (**b**) SEM image of N–S–CMK–3 800 °C, (**c**) comparative polarization curves for different catalysts with the same loading measured at 1600 rpm in O_2 saturated 0.1 M KOH solution, (**d**) HO_2^- yields (top) during the ORR and the corresponding electron transfer number (*n*, bottom) of the prepared catalysts measured by RRDE, adapted from [61].

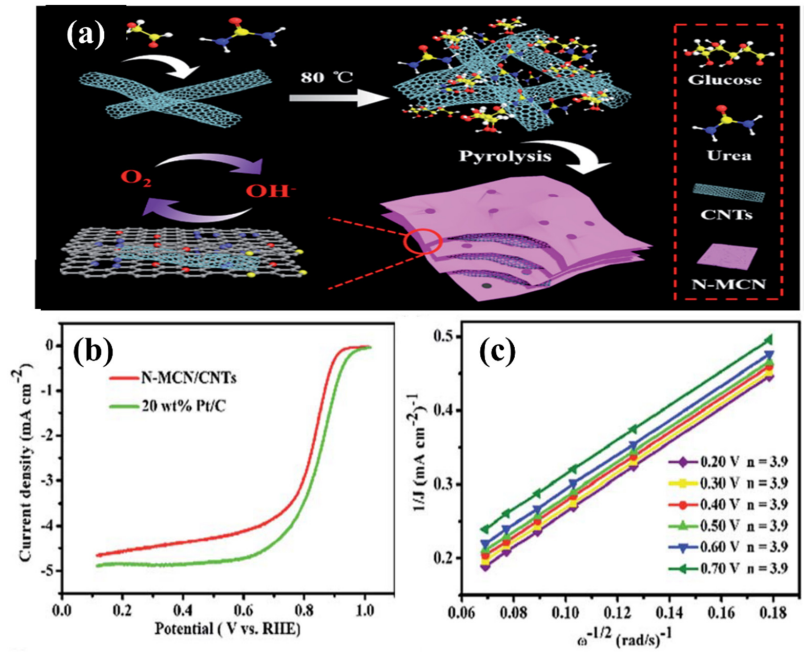

Figure 9. (**a**) Schematic for the synthesis of N-MCN/CNTs and the corresponding structural model, (**b**) LSV comparison of N-MCN/CNTs and Pt/C in an O_2-saturated 0.1 M KOH solution at a rotation rate of 1600 rpm, (**c**) K–L plots of N-MCN/CNTs at indicated potentials, adapted from [62].

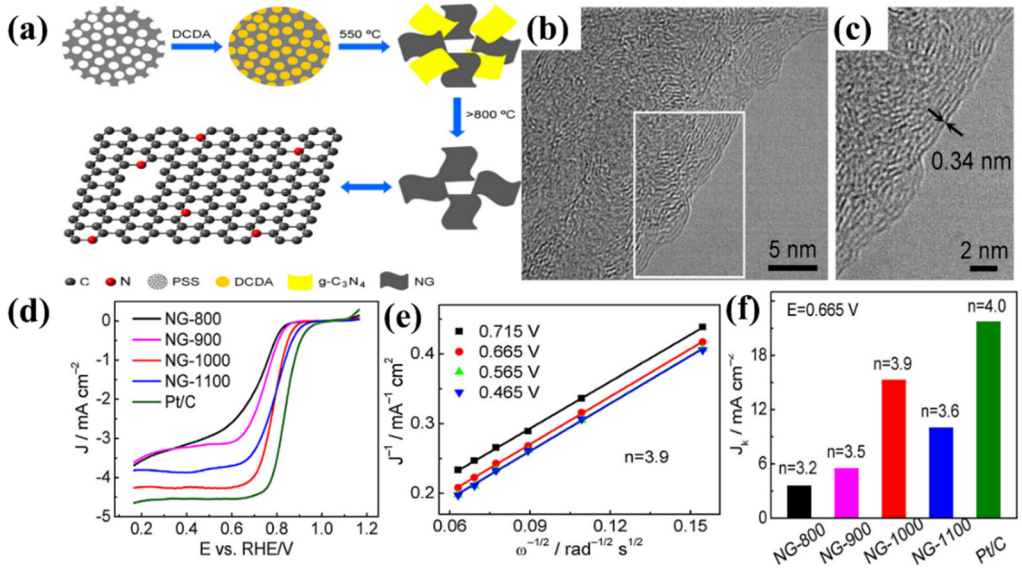

Figure 10. (**a**) Proposed synthetic mechanism for NG from PSS and DCDA, (**b**) high-resolution TEM images of NG–1000, and (**c**) the enlargement of the boxed area in (**b**), (**d**) LSV curves of different samples and Pt/C electrodes in O_2-saturated 0.1 M KOH solution with a sweep rate of 5 mV s^{-1} at a rotation rate of 1600 rpm, (**e**) K–L plots of NG–1000 at different potentials, (**f**) kinetic-limiting current density of NG and Pt/C catalysts, as well as the corresponding transferred electron numbers at 0.665 V, adapted from [73].

4.2. Plant-Based Biomass

Cellulose and its derivatives have recently been utilized more frequently than other types of biomasses to design highly active ORR electrocatalysts with a high percentage of carbon [18,74–80]. In addition, nitrogen/heteroatoms containing precursors are necessary to produce heteroatom-doped carbon with electroactive sites. For algae or soybean sources, the presence of proteins or other substances is very advantageous for heteroatom self-doping. Furthermore, the presence of salts might eliminate the necessity for activating agents or sacrificial templates since they function as pore-directing agents to generate pores following acid removal. Very recently a method was reported by Kaare et al. for the synthesis of N-doped carbon catalyst via a double pyrolysis method for the ORR from alder wood char (Figure 11a) [79]. The electrocatalytic ORR activity of wood-derived N-doped carbon (AWC–1) is noticeably higher than that of the most popular commercial carbon, XC-72R. AWC–1 shows an E_{onset} = 0.92 V vs. RHE, $E_{1/2}$ = 0.85 V vs. RHE, and J_L = 5.9 mA cm^{-2} (Figure 11b–d). The wood-derived catalyst's ORR activity was equivalent to that of the 20% Pt/C catalyst in 0.1 M KOH solution. Although after the second pyrolysis the BET surface area barely changed (2435 to 2245 m^2g^{-1}), the total volume of pores and the average pore diameter value both expanded. Authors have demonstrated that such electrocatalytic activity in alkaline media can be explained by the synergistic interplay between a large surface area (2245 m^2g^{-1}), high pore volume, and high pyridinic nitrogen content.

Very recently, M^+S^+C900–900 was developed from spinach leaves as a source of carbon, nitrogen, and iron, followed by a double heat treatment method (Figure 12a) [80]. According to the authors, the role of the second heat treatment is very crucial for the modulation of Fe-N active sites, porosity development (Figure 12b), as well as the overall enhancement of ORR activity. They have demonstrated that a second heat treatment might eliminate oxygen-containing functional groups and corrosive carbon species from the material surface and increase the degree of graphitization, which would then increase the ORR activity (Figure 12c). The as-prepared catalyst exhibits ORR catalytic activity with E_{onset} = 0.98 V vs. RHE, $E_{1/2}$ = 0.88 V vs. RHE, J_L = 5.8 mA cm^{-2}, and an *n* value of 3.91, which is superior to the other investigated catalysts (Figure 12d).

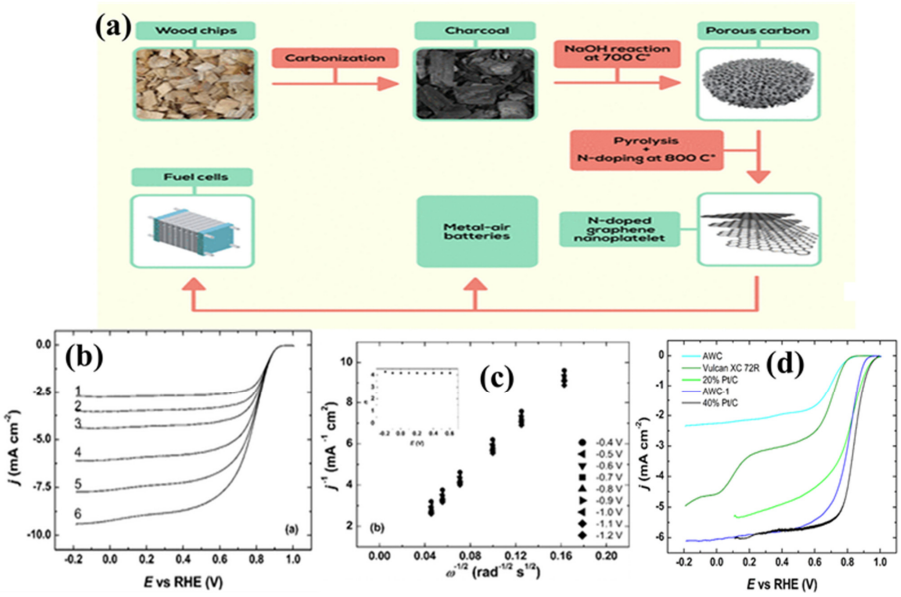

Figure 11. (**a**) Schematic diagram of N–doped carbon preparation, (**b**) RDE polarization curves of N–doped wood–based catalyst (AWC–1) in O_2–saturated 0.1 M KOH (ν = 10 mV s^{-1}, and ω = (1) 360, (2) 610, (3) 960, (4) 1900, (5) 3100, and (6) 4600 rpm), (**c**) K–L plots for ORR on a N–doped wood–based electrode in 0.1 M KOH at different potentials (inset: the changes of *n* values in the studied potential range), (**d**) LSV polarization curves of different catalyst in O_2–saturated 0.1 M KOH. ν = 10 mV s^{-1}, ω = 1900 rpm, adapted from [79].

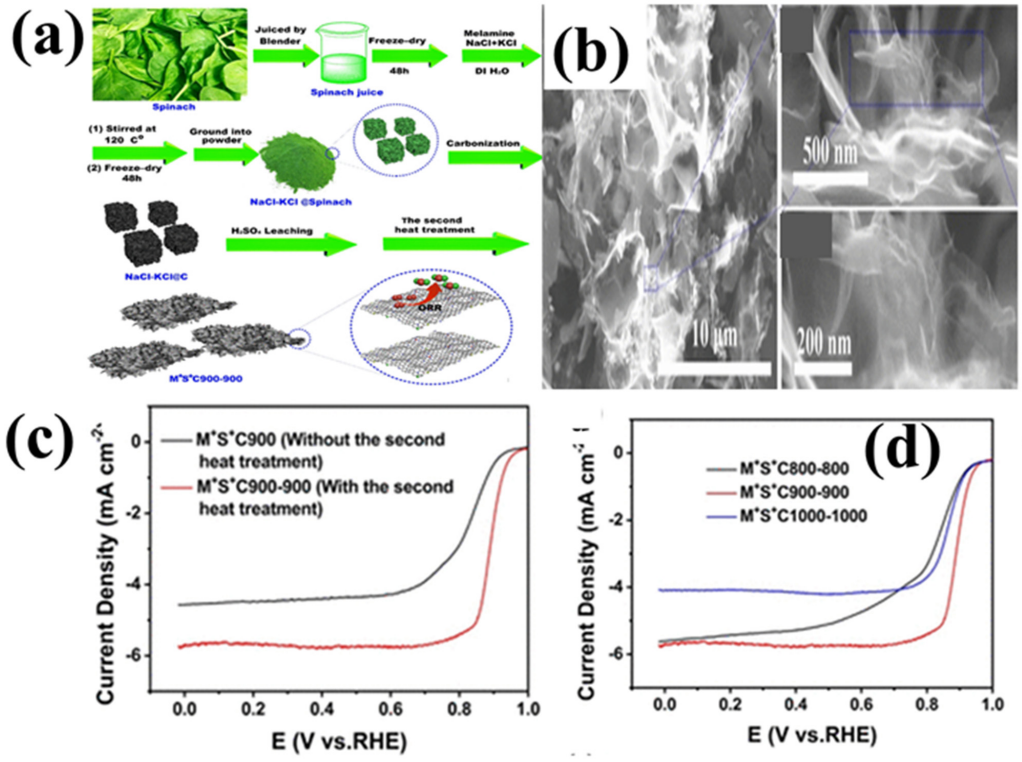

Figure 12. (**a**) Schematic of the procedure for preparing spinach-derived carbon nanosheets, (**b**) SEM images of M^+S^+C900–900, (**c**) effects of second heat treatment at 900 °C (**d**) effects of different reagents on the starting materials. (The LSV curves were recorded in O_2-saturated 0.1 M KOH with a rotation speed of 1600 rpm and a potential scan rate of 10 mV s^{-1}), adapted from [80].

5. Chitin and Chitosan-Based Biomass

The second most frequent natural biopolymers on earth are chitin and chitosan. These long, linear chain-like polysaccharide biopolymers are linked with functionalize surface groups via β-D glucosidic linkage. These biomaterials have exceptional physical and chemical properties due to their structural characteristics, which also exhibit low density and high porosity [81]. Without the use of extra N-dopant precursors, the high N concentration of chitin allows for its direct conversion into an N-doped carbon material [82–86].

Usage of starting material for the synthesis of carbon-based materials doped with Fe, N, S, and P which is very crucial for improving ORR performance. N, S, Fe–doped activated carbon was created by hydrothermal and pyrolytic chitin treatment at 950 °C, followed by $ZnCl_2$ activation (Figure 13a) [86]. $ZnCl_2$ is helpful for pore creation, as evidenced by the fact that the average pore size of the sample without $ZnCl_2$ addition is lower (0.90 nm) than that of the sample with $ZnCl_2$ addition (0.99 nm) which was further attributed to the improvement of catalytic activity. The XPS spectra showed that the BF–N–950 catalyst had N, Fe, and S doping levels of 5.14, 0.13, and 0.17 wt.%.

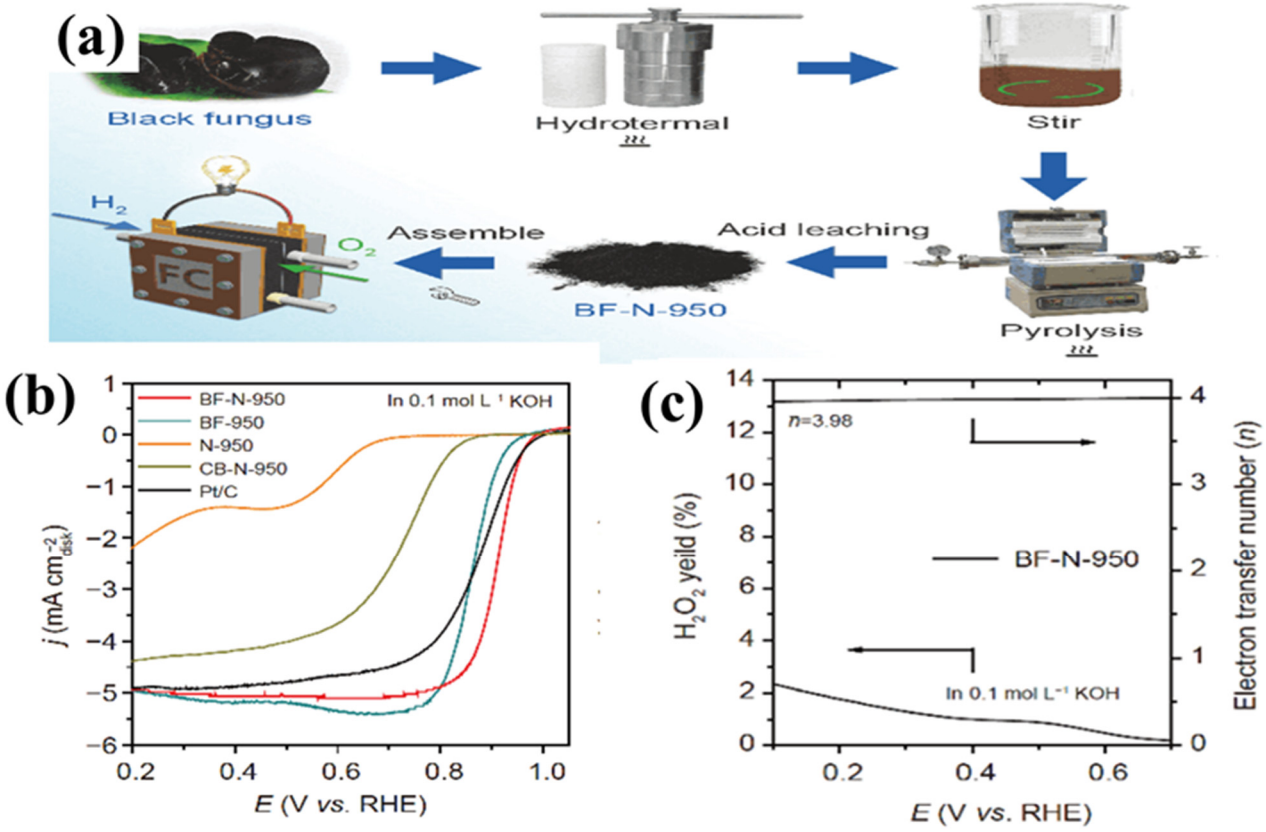

Figure 13. (**a**) Schematic illustration for the synthesis of BF–N–950 and fabrication of a PEMFC, (**b**) linear sweep voltammetry (LSV) polarization curves of the catalysts tested in O_2–saturated 0.1 mol L^{-1} KOH at a scan rate of 1 mV s^{-1}, (**c**) electron transfer number of the BF–N–950 in 0.1 M KOH, adapted from [86].

The rich Fe, N, S, and P in the black fungus raw materials as well as the additional N doping during the pyrolysis process were credited by the authors for the elevated ORR activity.

The BF–N–950 presented higher catalytic activity toward ORR with E_{onset} = 0.98 V vs. RHE, $E_{1/2}$ = 0.91 V vs. RHE, n = 3.99 (Figure 13b,c). Chitosan is an N-deacetylated derivative of chitin having a nitrogen content of about 7% and a degree of acetylation lower than 0.40 [87,88]. For ORR, chitosan-based biomass is a good candidate to synthesize metal-free carbon [89–93]. To create porous Co, N–doped graphene-like carbon nanosheets

(Co@N– PGCS) from chitosan, $Mg(OH)_2$ were also added during the nano casting process (Figure 14a) [90]. The resulting Co@N–PGCS had a mostly mesopore structure and a high specific surface area (1716 cm^2 g^{-1}). Here the metal oxide and magnesium oxide can act as hard templates, and then amorphous carbon from chitosan reorganized itself around the template. It exhibited similar ORR activity to Pt/C. Additionally, the current loss was very low (only 0.9%) after 10,000 s, which was far better than Pt/C (4.7%) and many other reported biomass-derived ORR electrocatalysts (Figure 14b). The as-fabricated catalyst exhibited ORR activity with $E_{1/2}$ = 0.84 V vs. RHE, J_L = 5.5 mA cm^{-2} (Figure 14c). The electron transfer number was reported to be 3.97, further confirming that the $4e^-$ reduction pathway was followed by the reaction.

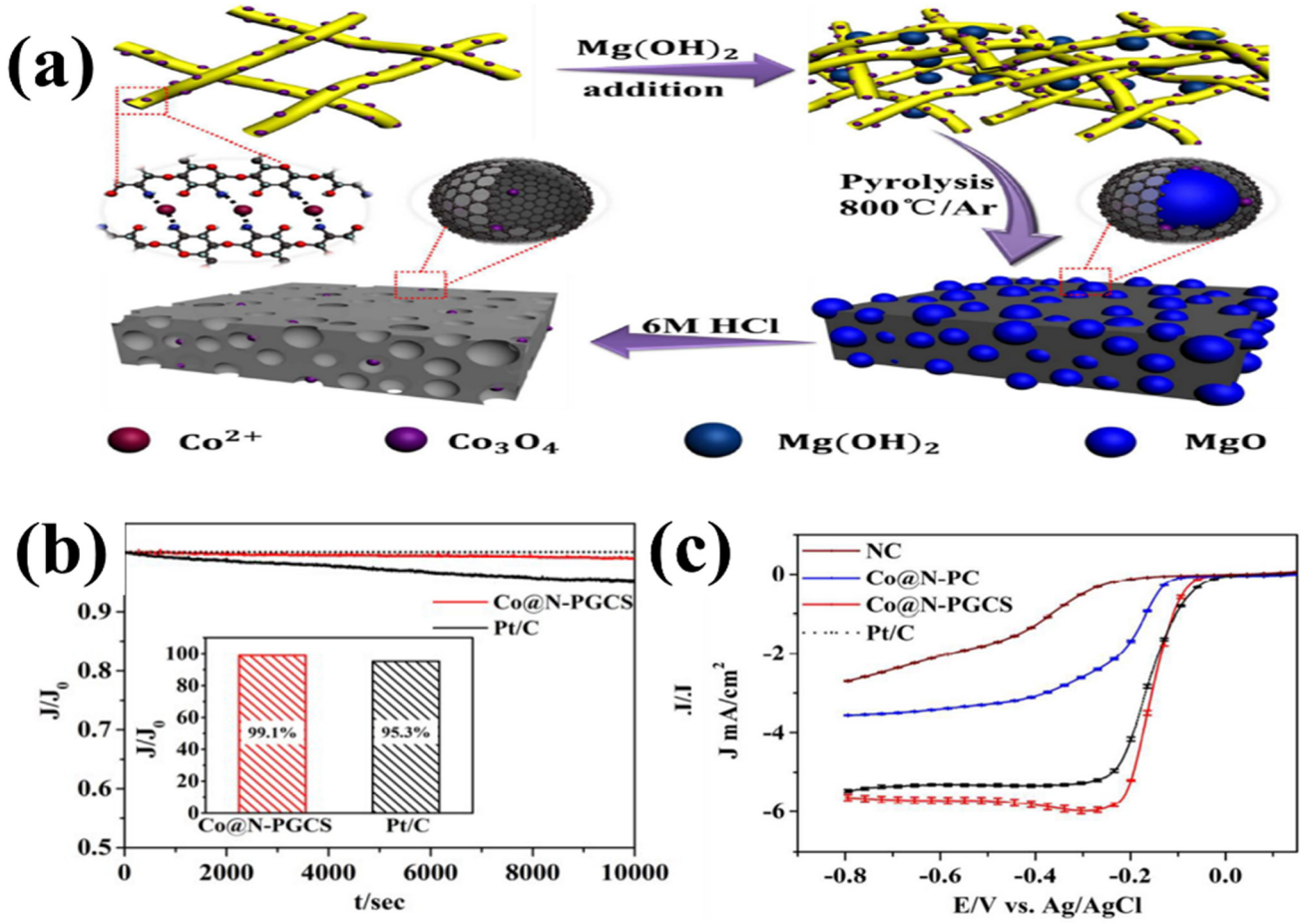

Figure 14. (**a**) Schematic illustration for the synthesis Co@N–PGCS, (**b**) stability curve, (**c**) linear sweep voltammetry (LSV) polarization curves of the catalysts tested in O_2–saturated 0.1 mol L^{-1} KOH, adapted from [90].

6. Lignin-Based Biomass

The first attempt to extract lignin was made in 1838 by a French scientist named Anselme Payen. After the treatment of concentrated nitric acid and sodium hydroxide, he obtained one insoluble fraction named cellulose and another dissolved portion was designated as lignin by Schulze [94]. Recently, Zhang et al. described the synthesis of N, S dual-doped carbon nanoplatelets via a pyrolysis method at 900 °C by using alkaline lignin (AL) as the carbon, sulfur source, and urea as the nitrogen source (Figure 15a) [95]. In this work, a one-step pyrolysis process was used to create S-doped or N, S co-doped carbon by taking the benefits of the sulfhydryl groups present in alkaline lignin. In alkaline conditions, ORR with 3.4 electron transfers was catalyzed by S-doped carbon that was produced at 900 °C and had just 0.67% sulfur. After the addition of urea, the ORR activity of formed N–S–C 900 dramatically increased with 3.8 electron transfer. The greater amount

of pyridinic-N and graphitic-N combined in N–S–C 900 (71.0%) greatly improves ORR performance (Figure 15b). It is ascribed that the two electrons of graphitic N and the one electron of pyridinic N present in the delocalized-π orbital have accelerated the flow of electrons from the carbon bands to the antibonding orbitals of O_2, which also enhances ORR. The as-prepared catalyst exhibits a positive shift of the onset potential (Figure 15b) to 0.97 V vs. RHE which is very close to Pt/C beside it also showed high stability of over 93.1% after 10,000 s (Figure 15c).

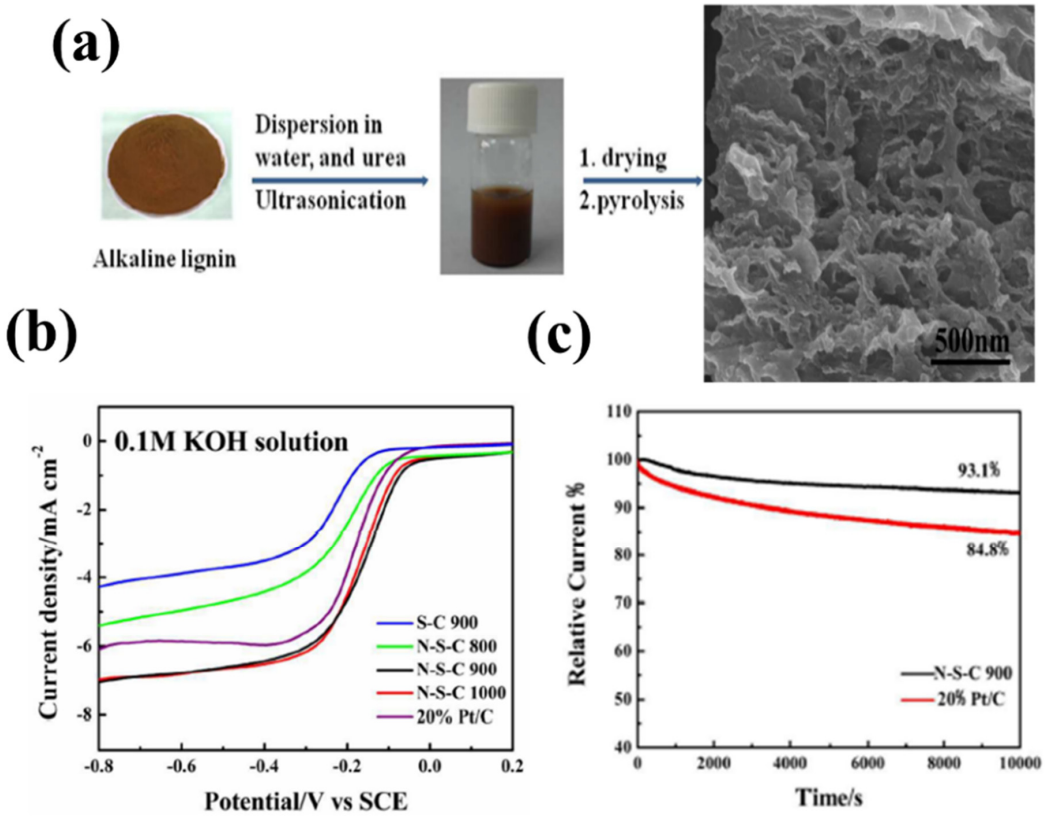

Figure 15. (**a**) The preparation procedure of N-S-C 900, (**b**) electrochemical activity studied using RRDE technique in an O_2-saturated 0.1 M KOH solution at 1600 rpm, (**c**) the stability curve of N-S-C 900 tested by the current-time chrono amperometric responses at 0.70 V versus RHE in O_2-saturated 0.1 M KOH solution, adapted from [95].

7. Conclusions and Future Perspective

Herein, different approaches for synthesizing carbon-based electrocatalysts from biomass and the key parameters influencing the physicochemical properties, as well as electrocatalytic activity, have been summarized (Table 1). It is important to mention that metal-free carbon-based materials, owing to their low cost of production, stability, and selectivity for the ORR, are ranked as suitable candidates for ORR. However, several challenges need to be addressed to design a robust electrocatalyst that can compete with the commercially available Pt/C electrocatalyst. First of all, the underlying mechanism behind the formation of carbon-based materials from different biomasses is yet to be properly understood. Secondly, the regulation of morphological features and the role of heteroatom doping on ORR activity need to be investigated to rationally design a highly active electrocatalyst utilizing biomass as the precursor. Moreover, carbon-based electrocatalysts show inferior ORR activity as well as stability in an acidic medium compared to the state-of-the-art Pt/C catalyst. So, for the proton exchange membrane fuel cell (PEMFC), carbon-based catalysts are not a proper choice and hence, modification such as surface functionalization is needed, which has rarely been studied. Overall, biomass-derived carbon-based electrocatalysts hold great promise in achieving remarkable electrocatalytic activity that will

ensure the development of various energy devices for commercial aspects. This review article would attract young researchers to devote themselves to designing more effective carbon-based electrocatalysts from biomass for ORR, which plays a crucial role in various energy conversion and storage devices.

Table 1. A list of ORR electrocatalysts derived from different types of biomass.

Biomass Source	Activation Method	Surface Area [m^2 g^{-1}]	E_{onset} [V] vs. RHE	$E_{1/2}$ [V] vs. RHE	J_L [mA cm^{-2}]	Transferred Electrons [*n*]	Ref.
Glucose	HTC, pyrolysis	1036	0.92	—	3.0	3.5–3.9	51
Glucose	Template-free, pyrolysis	450	0.90	0.79	4.10	—	46
Glucose	Hard templating, pyrolysis	1023	0.92	0.73	5.50	3.96	61
Glucose	Pyrolysis	591.4	0.95	0.82	4.7	3.9	62
Glucose	HTC, dual step pyrolysis	1610.3	0.99	0.87	5.8	4.0	63
Glucose	Dual template method	1148	0.97	0.87	5.5	—	60
Glucose	Pyrolysis	610	0.95	0.81	5.7	3.88	64
Glucose	HTC, pyrolysis	398	0.89	0.76	4.9	3.95	65
Glucose	Silica templating, dual step pyrolysis	801.5	0.94 *	0.87	5.1 *	4.0	66
Glucose	Soft templating, pyrolysis	480.5 cm^2 g^{-1}	0.92	0.81	5.01	3.62	67
Glucose	Dual templating, chemical activation	1394	0.94	0.824	4.4 *	3.20–3.97	68
Glucose(Bean curd)	Dual step pyrolysis	988.2	0.96	0.81	5.7	4.0	69
Sucrose	Co impregnation, carbonization	900	0.83 *	—	2.55	2.9–4.0 *	71
Sucrose	HTC, pyrolysis	528	0.88	0.74	5.6	3.72–3.9	72
Sucrose	HTC, pyrolysis	—	0.90 *	0.79	4.3 *	3.9	73
Bamboo fungus	HTC, pyrolysis	1895.5	1.08	0.92	3.5	3.6	18
Seaweed	Pyrolysis	1217	0.98	0.89	4.5 *	3.7	74
Okara	Pyrolysis	517	1.00	0.89	4	3.5	75
Grass	HTC, pyrolysis	—	0.91	—	5.2	3.94	76
Soybean shells	Carbonization, ammoxidation	1152	0.98	0.78	5.24	3.8	48
Eggplant	Activation, ammoxidation	1969	0.95	0.65	5.5	3.87	77
Coconut shells	Activation, pyrolysis	1071	0.84	—	5.4 *	3.7	78
Alder wood	Pyrolysis, ball milling	2245	0.92	0.85	5.9	—	79
Spinach	Freeze-dry, double pyrolysis	289.6	0.94 *	0.88	5.8 *	3.91	80
Chitin	HTC, pyrolysis	300.7	0.84	0.77 *	4.5	3.87–3.99	82
Chitin (Homarus americanus)	Pyrolysis	188	0.80 *	—	—	4	83
Chitin	Carbonization	76.18	0.80	—	4.64	3.65–3.87	84
Chitin	Chemical activation, pyrolysis	—	0.97	—	3.4 *	3.84	85
Chitin	HTC, pyrolysis	916	0.98 *	0.91	4.9 *	3.9	86
Chitosan	Pyrolysis	220	0.95	0.88	5.36	—	89
Chitosan	Hard templating, pyrolysis	1716	0.92	0.84	5.5 *	3.97	90
Chitosan	Double pyrolysis	416.7	0.94	0.90	3.58	3.2	91
Chitosan	Silica template method	873	0.92	0.82	3.3	3	92
Chitosan	Pyrolysis	337	0.91	0.82 *	6.92	3.25	93
Lignin	Pyrolysis	1209	0.97	0.87	6.9	3.8	95

The * marked data are evaluated from the figure.

Supplementary Materials: The following supporting information can be downloaded at: https://www.mdpi.com/article/10.3390/biomass2030010/s1, Figure S1: The schematic illustration of various modes of O_2 adsorption on catalyst surfaces: (a) on top end-on; (b) bridge end-on; (c) bridge side-on one site; and d, bridge side-on two sites, adapted from [28]. Figure S2: Trends in oxygen reduction activity plotted as a function of the oxygen-binding energy, adapted from [5]. Figure S3: Typical LSV polarization curve for ORR with different regions. Figure S4: Different forms of doped nitrogen in nitrogen-functionalized carbon, adapted from [3]. Figure S5: O_2 adsorption energy of all the doping configurations, adapted from [39].

Author Contributions: Conceptualization, S.D. and A.K.; methodology, S.D. and A.K.; writing—original draft preparation, S.D. and A.K.; writing—review and editing, S.G., T.K. and N.C.M.; supervision, A.K. All authors have read and agreed to the published version of the manuscript.

Funding: This research was funded by DST-INSPIRE Faculty Scheme, Department of Science and Technology, New Delhi, Govt. of India (IFA20-MS-168).

Acknowledgments: The authors are thankful to the Director, CSIR-Central Mechanical Engineering Research Institute, Durgapur.

Conflicts of Interest: The authors declare no conflict of interests.

References

1. Borghei, M.; Lehtonen, J.; Liu, L.; Rojas, O.J. Advanced biomass-derived electrocatalysts for the oxygen reduction reaction. *Adv. Mater.* **2018**, *30*, 1703691. [CrossRef]
2. Jasinski, R. A New Fuel cell cathode catalyst. *Nature* **1964**, *201*, 1212–1213. [CrossRef]
3. Yang, L.; Shui, J.; Du, L.; Shao, Y.; Liu, J.; Dai, L.; Hu, Z. Carbon-based metal-free ORR electrocatalysts for fuel cells: Past, present, and future. *Adv. Mater.* **2019**, *31*, 1804799. [CrossRef]
4. Chen, D.; Li, G.; Chen, X.; Zhang, Q.; Sui, J.; Li, C.; Zhang, Y.; Hu, J.; Yu, J.; Yu, L. Developing nitrogen and Co/Fe/Ni multi-doped carbon nanotubes as high-performance bifunctional catalyst for rechargeable zinc-air battery. *J. Colloid Interface Sci.* **2021**, *593*, 204–213. [CrossRef]
5. Seh, Z.W.; Kibsgaard, J.; Dickens, C.F.; Chorkendorff, I.B.; Nørskov, J.K.; Jaramillo, T.F. Combining theory and experiment in electrocatalysis: Insights into materials design. *Science* **2017**, *355*, eaad4998. [CrossRef]
6. Doan, T.L.L.; Tran, D.T.; Nguyen, D.C.; Kim, D.H.; Kim, N.H.; Lee, J.H. Rational engineering Co_xO_y nanosheets via phosphorous and sulfur dual-coupling for enhancing water splitting and Zn–air battery. *Adv. Funct. Mater.* **2021**, *31*, 2007822. [CrossRef]
7. Cui, Z.; Fu, G.; Li, Y.; Goodenough, J.B. Ni_3FeN-Supported Fe_3Pt intermetallic nano alloy as a high-performance bifunctional catalyst for metal-air batteries. *Angew Chem. Int. Ed.* **2017**, *56*, 9901–9905. [CrossRef]
8. Li, H.; Li, Q.; Wen, P.; Williams, T.B.; Adhikari, S.; Dun, C.; Lu, C.; Itanze, D.; Jiang, L.; Carroll, D.L. Colloidal cobalt phosphide nanocrystals as trifunctional electrocatalysts for overall water splitting powered by a zinc-air battery. *Adv. Mater.* **2018**, *30*, 1705796. [CrossRef]
9. Huang, S.-J.; Muneeb, A.; Sabhapathy, P.; Sheelam, A.; Bayikadi, K.S.; Sankar, R. Tailoring the Co^{4+}/Co^{3+} active sites in a single perovskite as a bifunctional catalyst for the oxygen electrode reactions. *Dalton Trans.* **2021**, *50*, 7212–7222. [CrossRef]
10. Shi, X.; Ling, X.; Li, L.; Zhong, C.; Deng, Y.; Han, X.; Hu, W. Nanosheets assembled into nickel sulfide nanospheres with enriched Ni^{3+} active sites for efficient water-splitting and zinc–air batteries. *J. Mater. Chem. A* **2019**, *7*, 23787–23793. [CrossRef]
11. Wang, Y.; Li, J.; Wei, Z. Recent progress of carbon-based materials in oxygen reduction reaction catalysis. *ChemElectroChem* **2018**, *5*, 1764–1774. [CrossRef]
12. Dhyani, V.; Bhaskar, T. A Comprehensive review on the pyrolysis of lignocellulosic biomass. *Renew. Energy* **2018**, *129*, 695–716. [CrossRef]
13. Wang, J.; Nie, P.; Ding, B.; Dong, S.; Hao, X.; Dou, H.; Zhang, X. Biomass derived carbon for energy storage devices. *J. Mater. Chem. A* **2017**, *5*, 2411–2428. [CrossRef]
14. Saini, S.; Chand, P.; Joshi, A. Biomass derived carbon for supercapacitor applications. *J. Energy Storage* **2021**, *39*, 102646. [CrossRef]
15. Chakraborty, R.; Vilya, K.; Pradhan, M.; Nayak, A.K. Recent advancement of biomass-derived porous carbon based materials for energy and environmental remediation applications. *J. Mater. Chem. A* **2022**, *10*, 6965–7005. [CrossRef]
16. Wei, Q.; Cherif, M.; Zhang, G.; Almesrati, A.; Chen, J.; Wu, M.; Komba, N.; Hu, Y.; Regier, T.; Sham, T.-K.; et al. Transforming reed waste into a highly active metal-free catalyst for oxygen reduction reaction. *Nano Energy* **2019**, *62*, 700–708. [CrossRef]
17. Kaur, P.; Verma, G.; Sekhon, S.S. Biomass derived hierarchical porous carbon materials as oxygen reduction reaction electrocatalysts in fuel cells. *Prog. Mater. Sci.* **2018**, *102*, 1–71. [CrossRef]
18. Gao, S.; Fan, H.; Zhang, S. Nitrogen-enriched carbon from bamboo fungus with superior oxygen reduction reaction activity. *J. Mater. Chem. A* **2014**, *2*, 18263–18270. [CrossRef]
19. Wang, N.; Li, T.; Song, Y.; Liu, J.; Wang, F. Metal-free nitrogen-doped porous carbons derived from pomelo peel treated by hypersaline environments for oxygen reduction reaction. *Carbon* **2018**, *130*, 692–700. [CrossRef]

20. Liu, L.; Zeng, G.; Chen, J.; Bi, L.; Dai, L.; Wen, Z. N-Doped porous carbon nanosheets as pH-universal ORR electrocatalyst in various fuel cell devices. *Nano Energy* **2018**, *49*, 393–402. [CrossRef]
21. Huang, B.; Liu, Y.; Guo, Q.; Fang, Y.; Titirici, M.-M.; Wang, X.; Xie, Z. Porous carbon nanosheets from biological nucleobase precursor as efficient pH-independent oxygen reduction electrocatalyst. *Carbon* **2020**, *156*, 179–186. [CrossRef]
22. Ghosh, S.; Santhosh, R.; Jeniffer, S.; Raghavan, V.; Jacob, G.; Nanaji, K.; Kollu, P.; Jeong, S.K.; Grace, A.N. Natural biomass derived hard carbon and activated carbons as electrochemical supercapacitor electrodes. *Sci. Rep.* **2019**, *9*, 1–15. [CrossRef]
23. Zhao, J.; Liu, Y.; Quan, X.; Chen, S.; Yu, H.; Zhao, H. Nitrogen-doped carbon with a high degree of graphitization derived from biomass as high-performance electrocatalyst for oxygen reduction reaction. *Appl. Surf. Sci.* **2017**, *396*, 986–993. [CrossRef]
24. Machan, C.W. Advances in the molecular catalysis of dioxygen reduction. *ACS Catal.* **2020**, *10*, 2640–2655. [CrossRef]
25. Katsounaros, I.; Cherevko, S.; Zeradjanin, A.R.; Mayrhofer, K.J.J. Oxygen electrochemistry as a cornerstone for sustainable energy conversion. *Angew. Chem. Int. Ed.* **2014**, *53*, 102–121. [CrossRef]
26. Rao, M.L.; Damjanovic, A.; Bockris, J.O. Oxygen adsorption related to the unpaired d-electrons in transition metals. *J. Phys. Chem.* **1963**, *67*, 2508–2509. [CrossRef]
27. Nørskov, J.K.; Rossmeisl, J.; Logadottir, A.; Lindqvist, L.; Kitchin, J.R.; Bligaard, T.; Jonsson, H. Origin of the overpotential for oxygen reduction at a fuel-cell cathode. *J. Phys. Chem. B* **2004**, *108*, 17886–17892. [CrossRef]
28. Worku, A.K.; Ayele, D.W.; Habtu, N.G. Recent advances and future perspectives in engineering of bifunctional electrocatalysts for rechargeable zinc–air batteries. *Mater. Today Adv.* **2021**, *9*, 100116. [CrossRef]
29. Lee, B.; Seo, H.R.; Lee, H.R.; Yoon, C.S.; Kim, J.H.; Chung, K.Y.; Cho, B.W.; Oh, S.H. Critical role of pH evolution of electrolyte in the reaction mechanism for rechargeable zinc batteries. *ChemSusChem* **2016**, *9*, 2948–2956. [CrossRef]
30. Ginting, R.T.; Ovhal, M.M.; Kang, J.-W. A novel design of hybrid transparent electrodes for high performance and ultra-flexible bifunctional electrochromic-supercapacitors. *Nano Energy* **2018**, *53*, 650. [CrossRef]
31. Stamenkovic, V.R.; Fowler, B.; Mun, B.S.; Wang, G.; Ross, P.N.; Lucas, C.A.; Markovic, N.M. Improved oxygen reduction activity on Pt_3Ni (111) via increased surface site availability. *Science* **2007**, *315*, 493–497. [CrossRef]
32. Levich, B. The theory of concentration polarisation. *Discuss. Faraday Soc.* **1947**, *1*, 37–49. [CrossRef]
33. Zhou, X.; Qiao, J.; Yang, L.; Zhang, J. A review of graphene-based nanostructural materials for both catalyst supports and metal-free catalysts in PEM fuel cell oxygen reduction reactions. *Adv. Energy Mater.* **2014**, *4*, 1301523. [CrossRef]
34. Kundu, A.; Samanta, A.; Raj, C.R. Hierarchical hollow MOF-derived bamboo-like N-doped carbon nanotube-encapsulated $Co_{0.25}Ni_{0.75}$ alloy: An efficient bifunctional oxygen electrocatalyst for zinc–air battery. *ACS Appl. Mater. Interfaces* **2021**, *13*, 30486–30496. [CrossRef]
35. Liu, X.; Dai, L. Carbon-based metal-free catalysts. *Nat. Rev. Mater.* **2016**, *1*, 1–12. [CrossRef]
36. Lai, L.; Potts, J.R.; Zhan, D.; Wang, L.; Poh, C.K.; Tang, C.; Gong, H.; Shen, Z.; Lin, J.; Ruoff, R.S. Exploration of the active center structure of nitrogen-doped graphene-based catalysts for oxygen reduction reaction. *Energy Environ. Sci.* **2012**, *5*, 7936–7942. [CrossRef]
37. Liu, J.; Song, P.; Xu, W. Structure-activity relationship of doped-Nitrogen (N)-based metal-free active sites on carbon for oxygen reduction reaction. *Carbon* **2017**, *115*, 763–772. [CrossRef]
38. Palm, I.; Kibena-Põldsepp, E.; Mooste, M.; Kozlova, J.; Käärik, M.; Kikas, A.; Treshchalov, A.; Leis, J.; Kisand, V.; Tamm, A. Nitrogen and phosphorus dual-doped silicon carbide-derived carbon/carbon nanotube composite for the anion-exchange membrane fuel cell cathode. *ACS Appl. Energy Mater.* **2022**, *5*, 2949–2958. [CrossRef]
39. Jiang, Y.; Yang, L.; Wang, X.; Wu, Q.; Ma, J.; Hu, Z. Doping sp^2 carbon to boost the activity for oxygen reduction in an acidic medium: A theoretical exploration. *RSC Adv.* **2016**, *6*, 48498–48503. [CrossRef]
40. Yang, D.-S.; Bhattacharjya, D.; Inamdar, S.; Park, J.; Yu, J.-S. Phosphorus-doped ordered mesoporous carbons with different lengths as efficient metal-free electrocatalysts for oxygen reduction reaction in alkaline media. *J. Am. Chem. Soc.* **2012**, *134*, 16127–16130. [CrossRef]
41. Zheng, X.; Luo, J.; Lv, W.; Wang, D.-W.; Yang, Q.-H. Two-dimensional porous carbon: Synthesis and ion-transport properties. *Adv. Mater.* **2015**, *27*, 5388–5395. [CrossRef]
42. Mi, J.; Wang, X.-R.; Fan, R.-J.; Qu, W.-H.; Li, W.-C. Coconut-shell-based porous carbons with a tunable micro/mesopore ratio for high-performance supercapacitors. *Energy Fuels* **2012**, *26*, 5321–5329. [CrossRef]
43. Du, L.; Xing, L.; Zhang, G.; Dubois, M.; Sun, S. Strategies for engineering high-performance PGM-free catalysts toward oxygen reduction and evolution reactions. *Small Methods* **2020**, *4*, 2000016. [CrossRef]
44. Guo, S.; Peng, J.; Li, W.; Yang, K.; Zhang, L.; Zhang, S.; Xia, H. Effects of CO_2 activation on porous structures of coconut shell-based activated carbons. *Appl. Surf. Sci.* **2009**, *255*, 8443–8449. [CrossRef]
45. Rodriguez-Reinoso, F.; Molina-Sabio, M. Activated carbons from lignocellulosic materials by chemical and/or physical activation: An overview. *Carbon* **1992**, *30*, 1111–1118. [CrossRef]
46. Fu, X.; Hu, X.; Yan, Z.; Lei, K.; Li, F.; Cheng, F.; Chen, J. Template-free synthesis of porous graphitic carbon nitride/carbon composite spheres for electrocatalytic oxygen reduction reaction. *Chem. Commun.* **2016**, *52*, 1725–1728. [CrossRef]
47. DB, M.S.; Desmecht, D.; Hima, H.I.; Mamane, O.S.; Natatou, I. Optimization of activated carbons prepared from parinari macrophylla shells. *Mater. Sci. Appl.* **2021**, *12*, 207–222.

48. Zhou, H.; Zhang, J.; Amiinu, I.S.; Zhang, C.; Liu, X.; Tu, W.; Pan, M.; Mu, S. Transforming waste biomass with an intrinsically porous network structure into porous nitrogen-doped graphene for highly efficient oxygen reduction. *Phys. Chem. Chem. Phys.* **2016**, *18*, 10392–10399. [CrossRef]
49. Wang, J.; Kaskel, S. KOH activation of carbon-based materials for energy storage. *J. Mater. Chem.* **2012**, *22*, 23710–23725. [CrossRef]
50. Guo, C.; Hu, R.; Liao, W.; Li, Z.; Sun, L.; Shi, D.; Li, Y.; Chen, C. Protein-enriched fish "biowaste" converted to three-dimensional porous carbon nano-network for advanced oxygen reduction electrocatalysis. *Electrochim. Acta* **2017**, *236*, 228–238. [CrossRef]
51. Liu, X.; Li, L.; Zhou, W.; Zhou, Y.; Niu, W.; Chen, S. High-performance electrocatalysts for oxygen reduction based on nitrogen-doped porous carbon from hydrothermal treatment of glucose and dicyandiamide. *ChemElectroChem* **2015**, *2*, 803–810. [CrossRef]
52. Wang, H.; Wang, K.; Song, H.; Li, H.; Ji, S.; Wang, Z.; Li, S.; Wang, R. N-doped porous carbon material made from fish-bones and its highly electrocatalytic performance in the oxygen reduction reaction. *RSC Adv.* **2015**, *5*, 48965–48970. [CrossRef]
53. Tam, M.S.; Antal, M.J. Preparation of activated carbons from macadamia nut shell and coconut shell by air activation. *Ind. Eng. Chem. Res.* **1999**, *38*, 4268–4276. [CrossRef]
54. Yuan, S.-J.; Dai, X.-H. Efficient sewage sludge-derived bi-functional electrocatalyst for oxygen reduction and evolution reaction. *Green Chem.* **2016**, *18*, 4004–4011. [CrossRef]
55. Alonso-Lemus, I.L.; Rodriguez-Varela, F.J.; Figueroa-Torres, M.Z.; Sanchez-Castro, M.E.; Hernandez-Ramirez, A.; Lardizabal-Gutierrez, D.; Quintana-Owen, P. Novel self-nitrogen-doped porous carbon from waste leather as highly active metal-free electrocatalyst for the ORR. *Int. J. Hydrogen Energy* **2016**, *41*, 23409–23416. [CrossRef]
56. Lin, G.; Ma, R.; Zhou, Y.; Liu, Q.; Dong, X.; Wang, J. KOH activation of biomass-derived nitrogen-doped carbons for supercapacitor and electrocatalytic oxygen reduction. *Electrochim. Acta* **2018**, *261*, 49–57. [CrossRef]
57. Zhou, X.; Zhu, Y.; Luo, W.; Ren, Y.; Xu, P.; Elzatahry, A.A.; Cheng, X.; Alghamdi, A.; Deng, Y.; Zhao, D. Chelation-assisted soft-template synthesis of ordered mesoporous zinc oxides for low concentration gas sensing. *J. Mater. Chem. A* **2016**, *4*, 15064–15071. [CrossRef]
58. Zhang, G.; Liu, X.; Wang, L.; Fu, H. Recent advances of biomass derived carbon-based materials for efficient electrochemical energy devices. *J. Mater. Chem. A* **2022**, *10*, 9277–9307. [CrossRef]
59. Wu, J.; Jin, C.; Yang, Z.; Tian, J.; Yang, R. Synthesis of phosphorus-doped carbon hollow spheres as efficient metal-free electrocatalysts for oxygen reduction. *Carbon* **2015**, *82*, 562–571. [CrossRef]
60. Kone, I.; Xie, A.; Tang, Y.; Chen, Y.; Liu, J.; Chen, Y.; Sun, Y.; Yang, X.; Wan, P. Hierarchical porous carbon doped with iron/nitrogen/sulfur for efficient oxygen reduction reaction. *ACS Appl. Mater. Interfaces* **2017**, *9*, 20963–20973. [CrossRef]
61. Qiu, Y.; Huo, J.; Jia, F.; Shanks, B.H.; Li, W. N-and S-Doped mesoporous carbon as metal-free cathode catalysts for direct biorenewable alcohol fuel cells. *J. Mater. Chem. A* **2016**, *4*, 83–95. [CrossRef]
62. Li, X.; Fang, Y.; Zhao, S.; Wu, J.; Li, F.; Tian, M.; Long, X.; Jin, J.; Ma, J. Nitrogen-doped mesoporous carbon nanosheet/carbon nanotube hybrids as metal-free bi-functional electrocatalysts for water oxidation and oxygen reduction. *J. Mater. Chem. A* **2016**, *4*, 13133–13141. [CrossRef]
63. Liu, F.; Liu, L.; Li, X.; Zeng, J.; Du, L.; Liao, S. Nitrogen self-doped carbon nanoparticles derived from spiral seaweeds for oxygen reduction reaction. *RSC Adv.* **2016**, *6*, 27535–27541. [CrossRef]
64. Li, Q.; Xu, D.; Ou, X.; Yan, F. Nitrogen-doped graphitic porous carbon nanosheets derived from in situ formed g-C_3N_4 templates for the oxygen reduction reaction. *Chem. Asian J.* **2017**, *12*, 1816–1823. [CrossRef] [PubMed]
65. Wei, W.; Ge, H.; Huang, L.; Kuang, M.; Al-Enizi, A.M.; Zhang, L.; Zheng, G. Hierarchically tubular nitrogen-doped carbon structures for the oxygen reduction reaction. *J. Mater. Chem. A* **2017**, *5*, 13634–13638. [CrossRef]
66. Luo, E.; Xiao, M.; Wang, Y.; Ge, J.; Liu, C.; Xing, W. Structural advantage induced by sulfur to boost the catalytic performance of FeNC catalyst towards the oxygen reduction reaction. *ChemCatChem* **2018**, *10*, 3653–3658. [CrossRef]
67. Zhang, L.; Qi, C.; Zhao, A.; Xu, G.; Xu, J.; Zhang, L.; Zhang, C.; Jia, D. N-doped porous carbon-encapsulated Fe nanoparticles as efficient electrocatalysts for oxygen reduction reaction. *Appl. Surf. Sci.* **2018**, *445*, 462–470. [CrossRef]
68. Li, X.; Guan, B.Y.; Gao, S.; Lou, X.W.D. A general dual-templating approach to biomass-derived hierarchically porous heteroatom-doped carbon materials for enhanced electrocatalytic oxygen reduction. *Energy Environ. Sci.* **2019**, *12*, 648–655. [CrossRef]
69. Zheng, H.; Zhang, Y.; Long, J.; Li, R.; Gou, X. Nitrogen-doped porous carbon material derived from biomass of beancurd as an efficient electrocatalyst for oxygen reduction and Zn-air fuel cell. *J. Electrochem. Soc.* **2020**, *167*, 084516. [CrossRef]
70. Ryoo, R.; Joo, S.H.; Jun, S. Synthesis of highly ordered carbon molecular sieves via template-mediated structural transformation. *J. Phys. Chem. B* **1999**, *103*, 7743–7746. [CrossRef]
71. Bo, X.; Guo, L. Ordered mesoporous boron-doped carbons as metal-free electrocatalysts for the oxygen reduction reaction in alkaline solution. *Phys. Chem. Chem. Phys.* **2013**, *15*, 2459–2465. [CrossRef]
72. Sun, Y.; Wu, J.; Tian, J.; Jin, C.; Yang, R. Sulfur-Doped carbon spheres as efficient metal-free electrocatalysts for oxygen reduction reaction. *Electrochim. Acta* **2015**, *178*, 806–812. [CrossRef]
73. Pan, F.; Guo, S.; Zhang, J. Swelling-induced synthesis of nitrogen-doped graphene for oxygen reduction reaction. *Electrochim. Acta* **2015**, *180*, 29–36. [CrossRef]
74. Song, M.Y.; Park, H.Y.; Yang, D.-S.; Bhattacharjya, D.; Yu, J.-S. Seaweed-derived heteroatom-doped highly porous carbon as an electrocatalyst for the oxygen reduction reaction. *ChemSusChem* **2014**, *7*, 1755–1763. [CrossRef] [PubMed]
75. Wang, R.; Wang, H.; Zhou, T.; Key, J.; Ma, Y.; Zhang, Z.; Wang, Q.; Ji, S. The enhanced electrocatalytic activity of okara-derived N-doped mesoporous carbon for oxygen reduction reaction. *J. Power Sources* **2015**, *274*, 741–747. [CrossRef]

76. Zhang, H.; Chen, J.; Li, Y.; Liu, P.; Wang, Y.; An, T.; Zhao, H. Nitrogen-doped carbon nanodots@nanospheres as an efficient electrocatalyst for oxygen reduction reaction. *Electrochim. Acta* **2015**, *165*, 7–13. [CrossRef]
77. Zhou, H.; Zhang, J.; Zhu, J.; Liu, Z.; Zhang, C.; Mu, S. A self-template and KOH activation co-coupling strategy to synthesize ultrahigh surface area nitrogen-doped porous graphene for oxygen reduction. *RSC Adv.* **2016**, *6*, 73292–73300. [CrossRef]
78. Borghei, M.; Laocharoen, N.; Kibena-Põldsepp, E.; Johansson, L.-S.; Campbell, J.; Kauppinen, E.; Tammeveski, K.; Rojas, O.J. Porous N, P-doped carbon from coconut shells with high electrocatalytic activity for oxygen reduction: Alternative to Pt-C for alkaline fuel cells. *Appl. Catal. B Environ.* **2017**, *204*, 394–402. [CrossRef]
79. Kaare, K.; Yu, E.; Volperts, A.; Dobele, G.; Zhurinsh, A.; Dyck, A.; Niaura, G.; Tamasauskaite-Tamasiunaite, L.; Norkus, E.; Andrulevičius, M. Highly active wood-derived nitrogen-doped carbon catalyst for the oxygen reduction reaction. *ACS Omega* **2020**, *5*, 23578–23587. [CrossRef]
80. Liu, X.; Culhane, C.; Li, W.; Zou, S. Spinach-derived porous carbon nanosheets as high-performance catalysts for oxygen reduction reaction. *ACS Omega* **2020**, *5*, 24367–24378. [CrossRef]
81. Peter, S.; Lyczko, N.; Gopakumar, D.; Maria, H.J.; Nzihou, A.; Thomas, S. Chitin and chitosan based composites for energy and environmental applications: A review. *Waste Biomass Valorization* **2021**, *12*, 4777–4804. [CrossRef]
82. Yuan, H.; Deng, L.; Cai, X.; Zhou, S.; Chen, Y.; Yuan, Y. Nitrogen-doped carbon sheets derived from chitin as non-metal bifunctional electrocatalysts for oxygen reduction and evolution. *RSC Adv.* **2015**, *5*, 56121–56129. [CrossRef]
83. Preuss, K.; Kannuchamy, V.K.; Marinovic, A.; Isaacs, M.; Wilson, K.; Abrahams, I.; Titirici, M.-M. Bio-inspired carbon electrocatalysts for the oxygen reduction reaction. *J. Energy Chem.* **2016**, *25*, 228–235. [CrossRef]
84. Wang, B.; Li, S.; Wu, X.; Liu, J.; Chen, J. Biomass chitin-derived honeycomb-like nitrogen-doped carbon/graphene nanosheet networks for applications in efficient oxygen reduction and robust lithium storage. *J. Mater. Chem. A* **2016**, *4*, 11789–11799. [CrossRef]
85. Yao, L.; Zhong, W.; Qiu, L.; Deng, L. Nitrogen-doped porous carbon derived from chitin with enhanced performances for oxygen reduction reaction and supercapacitor. *Int. J. Electrochem. Sci.* **2018**, *13*, 5798–5809. [CrossRef]
86. Wang, X.; Fang, J.; Liu, X.; Zhang, X.; Lv, Q.; Xu, Z.; Zhang, X.; Zhu, W.; Zhuang, Z. Converting biomass into efficient oxygen reduction reaction catalysts for proton exchange membrane fuel cells. *Sci. China Mater.* **2020**, *63*, 524–532. [CrossRef]
87. Kumar, M.N.R. A review of chitin and chitosan applications. *React. Funct. Polym.* **2000**, *46*, 1–27. [CrossRef]
88. Rinaudo, M. Chitin and chitosan: Properties and applications. *Prog. Polym. Sci.* **2006**, *31*, 603–632. [CrossRef]
89. Xie, S.; Huang, S.; Wei, W.; Yang, X.; Liu, Y.; Lu, X.; Tong, Y. Chitosan waste-derived Co and N Co-doped carbon electrocatalyst for efficient oxygen reduction reaction. *ChemElectroChem* **2015**, *2*, 1806–1812. [CrossRef]
90. Liu, X.; Amiinu, I.S.; Liu, S.; Cheng, K.; Mu, S. Transition Metal/Nitrogen dual-doped mesoporous graphene-like carbon nanosheets for the oxygen reduction and evolution reactions. *Nanoscale* **2016**, *8*, 13311–13320. [CrossRef]
91. Wang, W.; Liu, S.; Liu, Y.; Jing, W.; Zhao, R.; Lei, Z. Phenolic resin/chitosan composite derived nitrogen-doped carbon as highly durable and anti-poisoning electrocatalyst for oxygen reduction reaction. *Int. J. Hydrogen Energy* **2017**, *42*, 26704–26712. [CrossRef]
92. Guo, D.; Wei, H.; Chen, X.; Liu, M.; Ding, F.; Yang, Z.; Yang, Y.; Wang, S.; Yang, K.; Huang, S. 3D hierarchical nitrogen-doped carbon nanoflower derived from chitosan for efficient electrocatalytic oxygen reduction and high performance lithium–sulfur batteries. *J. Mater. Chem. A* **2017**, *5*, 18193–18206. [CrossRef]
93. Zhang, Y.; Lu, L.; Zhang, S.; Lv, Z.; Yang, D.; Liu, J.; Chen, Y.; Tian, X.; Jin, H.; Song, W. Biomass chitosan derived cobalt/nitrogen doped carbon nanotubes for the electrocatalytic oxygen reduction reaction. *J. Mater. Chem. A* **2018**, *6*, 5740–5745. [CrossRef]
94. McCarthy, J.L.; Islam, A. Lignin chemistry, technology, and utilization: A brief history. *ACS Symp. Ser.* **2000**, *742*, 2–99.
95. Zhang, X.; Yu, D.; Zhang, Y.; Guo, W.; Ma, X.; He, X. Nitrogen-and sulfur-doped carbon nanoplatelets via thermal annealing of alkaline lignin with urea as efficient electrocatalysts for oxygen reduction reaction. *RSC Adv.* **2016**, *6*, 104183–104192. [CrossRef]